Fiber Optic Methods for Nondestructive Testing

by
Sridhar Rudraraju

Thesis submitted to the Faculty of the
Virginia Polytechnic Institute and State University
in the partial fulfillment of the requirements for the degree of

MASTER OF SCIENCE
in
Electrical Engineering

APPROVED:

Richard O. Claus, Chairman

Anbo Wang

Kent A. Murphy

August, 1994

Blacksburg, Virginia

Fiber Optic Methods for Nondestructive Testing

by
Sridhar Rudraraju

Richard O. Claus, Chairman
Electrical Engineering
(ABSTRACT)

This thesis demonstrates the use of fiber optic methods for nondestructive testing of composite materials and aluminum specimens using the acousto-ultrasound approach. A noncontact method using a hybrid interferometer is devised for measuring absolute surface acoustic wave (SAW) amplitudes. The J1..J4 spectrum analysis technique is used for calibrating the piezoelectric transducer cylinder (PZT) and J0/J2 spectrum analysis technique is used for demodulating the SAW signal from the interferometer. An extrinsic Fabry-Perot interferometric (EFPI) sensor is utilized for sensing acoustic emission, measuring speed and attenuation in aluminum and composite specimens. A broadband preamplifier is designed for amplifying signals from the EFPI sensor. Theoretical and practical minimum detectable air gap change of an EFPI sensor are calculated for the system. The directional sensitivity of the EFPI sensor to SAW is studied.

Acknowledgments

I gratefully acknowledge the guidance and support provided by my advisor, Dr. Richard O Claus during my graduate career. His insight and wisdom were invaluable to this thesis. I would like to thank my committee members, Dr. Anbo Wang, and Dr. Kent A. Murphy for their helpful suggestions and constant encouragement.

I owe a great deal of thanks to the members of the Fiber and Electro-Optic Research Center (FEORC) and Dr. S. Sudarshanam who provided support, assistance and valuable suggestions in the progress of this research.

I acknowledge FFA-Aeronautical Research Institute of Sweden for funding this research.

Finally, I am indebted to my family, especially my parents Satyanarayana Raju Rudraraju and Vijayalakshmi Rudraraju, and my brother Giridhar Rudraraju, for the love and support they extended to me.

Table of Contents

List of Figures

List of Tables

Chapter 1 - Introduction

1.1 Background

Composite materials are being extensively used in industry and at home because of their light weight, resistance to corrosion, high strength, and reliability at high temperatures. With the increasing use of composite materials in engineering structures there is a growing need of techniques for detecting and analyzing their flaws, damage, and defects. The analysis of these parameters is necessary to enhance the lifetime and examine the operability of engineering structures. Over the years nondestructive testing (NDT) has proved to be a vital technique in the study of damage development in composite materials (matrix cracks, fiber matrix disbonds, delamination, cracks). NDT is also increasingly used in quality assurance, control of manufactured products, and industrial and environmental safety. NDT is basically a method for testing and evaluating engineering materials and their properties. Several NDT methods have been developed for studying the properties of composite materials, each having its own advantages and disadvantages. One of the problems with NDT is that there is a choice of innumerable approaches, with no universal

method for all applications. The choice of a particular NDT method is decided by the operator and depends on the defect sensitivity, capital costs, speed of operation, maintenance costs, and overall reliability. A number of NDT methods exist[1.1] and they are listed below.

1. *Visual methods*: The visual method involves the inspection of the surface of the material. Surface cracks are the most common form of damage in engineering structures. A simple inspection by the naked eye or with a microscope is a visual aid for NDT. Optical holography and speckle pattern interferometry are also finding increasing use for capturing the surface information from materials. The advent of computers has led to high speed scanning, storage and retrieval of digital data thus enabling automation of the testing process. Miniaturized cameras and films have also been developed for attachment inside pipes and various other structures to detect surface cracks.

2. *Radiological methods*: X rays and gamma rays have been used for NDT because of their high directivity and ability to travel in straight lines, penetration of thick materials with partial absorption, wide waveband and the ease of capturing them on photographic films. X rays, after traversing through the specimen under test, can be recorded by radiographic films, intensifying screens, fluorescent screens, ionization gauges, and scintillation counters revealing information about cracks and flaws inside the material. Both uniform and non uniform thickness specimens, castings and assemblies can be tested using various radiographic techniques. Fully automated X ray testing of cast parts has also been demonstrated [1.2].

3. *Ultrasonic testing method*: This is one of the most popular forms of NDT techniques for the detection of internal flaws and thickness of specimens. In this method, high frequency

pulses are launched into the specimen under test by a piezoelectric transducer (PZT) to induce mechanical vibrations. These waves propagate through the material with a certain amount of attenuation and scatter at an internal flaw. The scattered and reflected waves from the edges of the specimen are detected by using a suitable sensor or another PZT. The ultrasonic signals are usually captured in the time domain, and the difference in arrival times between the transmitted and reflected signals is directly related to the dimension of the specimen, and hence may be used to determine thickness of the specimen under test. Moreover, the magnitude of the scattered signal reveals information about the size of the flaw. Ultrasonic testing methods have also been used for characterizing the curing of epoxies [1.3].

4. *Magnetic method*: This method is only applicable for materials that can be strongly magnetized (ferromagnetic) and is mainly used for the detection of surface cracks. In this technique, the specimen is magnetized causing the magnetic lines of force to be evenly distributed in the material. In case of a crack, however, there is a distortion in the field causing local magnetic flux leakage fields due to sudden local changes in permeability. These leaks can then be detected by spraying powdered magnetic particles or by using liquid magnetic ink. The cracks can then be detected visually due to the accumulation of the magnetic material at the sites of the cracks.

5. *Electrical methods*: These techniques are mostly used where external contact with the specimen is undesirable. They are indirect methods since the material property is correlated with the appropriate electromagnetic properties. The two main methods used in this NDT technique are the eddy current method and the potential drop method. In the eddy current method alternating current is passed through coils acting as probes that can be moved across the surface, or can encircle the metal specimen. When the magnetic fields induced

by the coils, interacts with the electrically conducting specimen, it produces eddy currents in the specimen. These, in turn, produce a magnetic field opposing the field in the coil, thus decreasing the magnetic flux. The reduction of the magnetic flux causes a change in the impedance of the coil which can be measured and correlated to the material property being measured. In the potential drop method the potential difference between a pair of contacts placed on the surface of a specimen carrying current is measured, the potential difference varying for different points on the specimen and as a function of size and location of a flaw.

6. *Penetration flaw detection method*: This technique is an extension of the visual method for detecting surface cracks that appear small externally but are large inside the material. Special liquids known as penetrant liquids are smeared over the surface of the specimen to penetrate the openings in the cracks. The surface is then cleaned thoroughly and sprayed with a developer. After some time the penetrant is absorbed by the developer at the crack openings, thus revealing the locations of the flaws. The choice of the penetrant is dependent on its surface tension, density, and wetting properties rather than upon viscosity. Fluorescent and visible dye are used as developers.

7. *Acoustic emission methods*: High frequency sound waves (20 kHz to 30 MHz) are emitted in a material when it is subjected to large amounts of stress. These stress waves are known as acoustic waves and the phenomenon is known as acoustic emission (AE). Acoustic waves are believed to originate due to sudden localized stress in a region causing sudden bursts of energy that travel through the material to the surface. The acoustic signals can be detected by conventional piezoelectric transducers which can convert the mechanical vibration into electrical energy or by other types of sensors. AE is now being used

extensively as an NDT technique for determining the location of a crack, size of the crack, and crack propagation.

1.2 Acousto-ultrasonic approach

Ultrasonic testing and acoustic emission methods for nondestructive evaluation (NDE) of laminated and fiber reinforced composites are developing rapidly and are being widely accepted in the industry over many other NDT techniques. The acousto-ultrasonic approach combines the inherent advantages of both the ultrasonic testing and the acoustic emission techniques for NDE of composites to determine the reliability of engineering structures and materials. The term "Acousto-ultrasonic" can be taken as a contraction of "acoustic emission simulation with ultrasonic sources" [1.4]. In this method stress waves similar to the ones encountered in an acoustic emission event, as a result of loading or crack propagation are simulated and induced onto the specimen under test. The simulated ultrasonic stress waves propagate through the material, and are modulated by the properties of the material. The modulated signals are studied and related to the flaws and properties of the material.

Unlike loading the specimen to generate acoustic emission events in the acoustic technique, stress waves are simulated in the material without disrupting it in the acousto-ultrasonic technique . Moreover, the acousto-ultrasound approach deals with the combined effects of any defects in the material such as broken fibers, delamination, local porosity, and resign rich areas, rather than flaw detection. It then asscsses the variation in the material properties that determine the strength and toughness of the material, by integrating the effects of various kinds of defects. In conventional acoustic emission methods the nature and location of the vibrations is unknown. In contrast, the nature and location of the

acoustic emission source is usually fixed in the acousto-ultrasonic approach. It is more viable where conventional ultrasonic testing methods are impractical to use and pulse-echo methods impose constraints.

The acousto-ultrasound approach consists of two transducers which are separated by a known distance, the first to generate the acoustic signals and the other to detect the signals. Usually conventional piezoelectric transducers are used to generate and receive the acoustic signals by attaching them to the surface or the edge of the specimen. However, other kinds of sources and sensors such as laser [1.5], pencil lead break [1.6], and fiber optic sensors [1.7] may also be used. Single frequency pulses or broadband signals generated by a pulse generator or a signal generator are used to drive the source transducer. The signals received by the second transducer are amplified using a broadband preamplifier before they are analyzed on the oscilloscope. Fig. 1.1 illustrates the schematic of the instrumentation and basic arrangement used for the NDE of composite materials.

The acoustic waves are more complex in the acousto-ultrasonic approach since they are modulated by the various material properties of the specimen, unlike a series of isolated echoes in the pulse-echo ultrasonic method. The transducer is coupled to the specimen with fluid couplants (glycerin, gel, silicone grease) and dry couplants (silicone rubber) in order to achieve maximum transfer of acoustic energy. The sensing transducer can be placed at various points on the specimen to determine the properties of various regions of the specimen . The variations in the material properties are measured and quantified in terms of the stress wave factor (SWF) [1.8] which is defined in many ways such as ringdown count, peak voltage, signal rise time, and energy. In the ringdown method the SWF is defined as the number of ringdown oscillations per waveform measured above a threshold voltage, which is usually set just above the noise floor. Peak voltage SWF

measures the peak to peak voltage of the signal detected by the receiving transducer. The SWF can also be defined based on the energy (given by the square of root mean square voltage). Usually the SWF values are normalized to correlate to the material property variation.

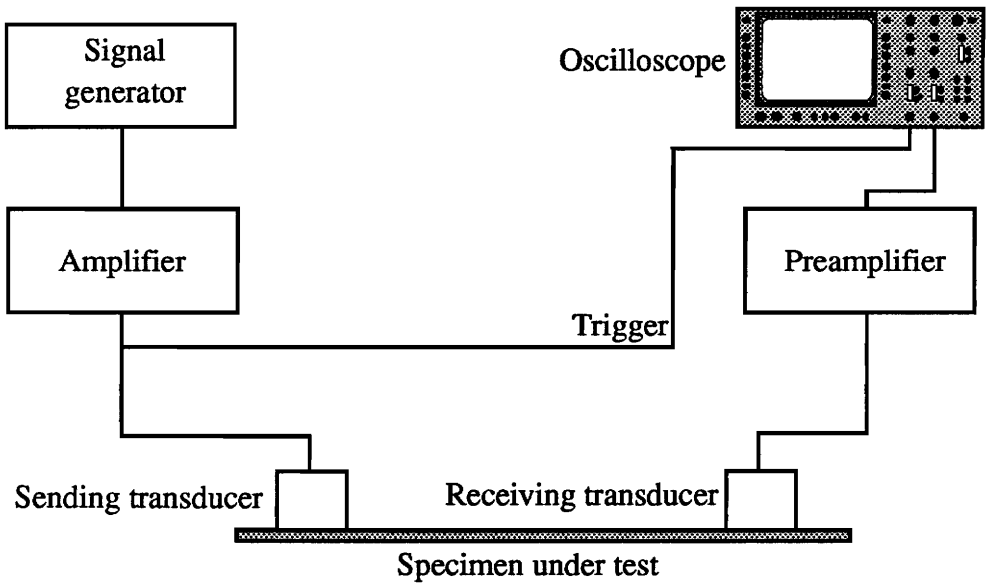

Figure 1.1. Schematic of the basic instrumentation and arrangement used in the acousto-ultrasonic approach.

Chapter 2 - Fiber optic sensors

2.1 Introduction

Fiber optic sensors are rapidly replacing existing conventional electrical and mechanical sensors and are finding a permanent place in industry. Optical fiber sensors owe this enormous growth to two factors: reduced cost and superior performance. With a surge in the application of fiber optics in the telecommunications industry, the cost of fiber components and opto-electronic devices, essential for fiber sensors, is drastically reducing. Superior performance coupled with technological advancements led to the wide use of fiber optic sensors for measuring environmental parameters such as strain, pressure, vibration, acceleration, electric fields, magnetic fields, rotation, temperature, current and acoustics [2.1].

Optical fiber sensors offer several advantages over their electronic counterparts:

- Light weight and small size,
- Immunity to electromagnetic interference,

- Wide bandwidth,
- High sensitivity,
- Environmental ruggedness,
- Multiplexing capability,
- Large temperature sustenance, and
- Ease of embedding,

Because of these inherent advantages, fiber sensors are also finding increasing use in novel technologies like Smart Materials and Structures, and Intelligent Vehicles and Highway Systems (IVHS). In Smart Materials and Skins, the sensors are embedded into the structure for monitoring the long term health of the systems [2.2]. Such on-line monitoring is utilized for maintenance of the engineering structures, thus, enhancing the life time of the structures. In IVHS, sensors are embedded in the highway for monitoring traffic flow, speed of vehicles, and weight in motion, thus playing a significant role in traffic management.

2.2 Classification

Various types of fiber sensors have been cited in the literature [2.3]. Optical fiber sensors can be broadly classified into intrinsic and extrinsic fiber optic sensors depending on whether the sensing region is inside or outside the fiber respectively. Other important subclasses are intensity modulated and phase modulated or interferometric sensors, depending upon how the guided light through the optical fiber is modulated by external perturbation. Fig. 2.1 illustrates different types of extrinsic and intrinsic based fiber sensors and their applications.

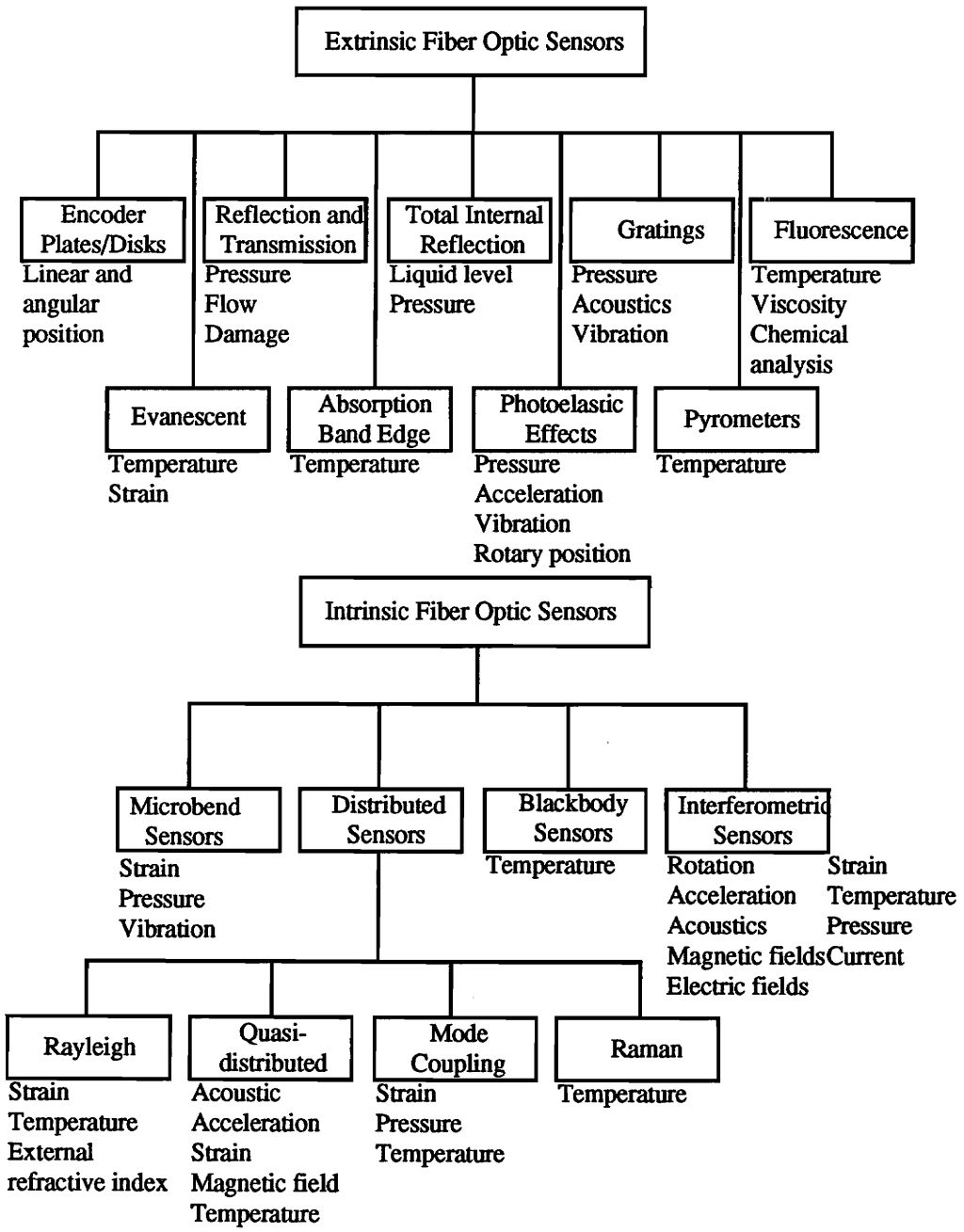

Figure 2.1. Classification of fiber optic sensors [2.4].

2.2.1 Intensity based sensors

In intensity based sensors the intensity of the guided light through the optical fiber is modulated by the external disturbance. However, variation in intensity of the transmitted light in the fiber is considerably less susceptible small environmental changes, henceforth reducing the noise. Also, significant modifications of the fiber are necessary for the fabrication of optical intensity sensors. Several of the fiber intensity sensor configurations have been proposed [2.1,2.4,2.5]. Compared to interferometric sensors, intensity based sensors tend to emphasize electrical passiveness, electromagnetic noise immunity, ruggedness, and versatility rather than higher sensitivity.

Fiber optic intensity sensors can be further classified into hybrid and internal effect sensors depending upon whether the light intensity is modulated inside or outside the optical fiber [2.4]. Fig. 2.2(a) shows the classification of fiber optic intensity sensors. Hybrid sensors require special miniaturized devices at the endface of the fiber to modulate the intensity of the light. These devices are of various sizes and materials. In internal effect sensors, however, the intensity is modulated by the physical dimensions of the fiber itself via mechanical manipulation.

Hybrid fiber optic sensors are the largest class of fiber sensors because of the great variety of devices that can be attached to the sensors. Hybrid sensors can be further classified as light valve, scattering or the spectral sensors. In light valve sensors, the light exiting from the source fiber is intensity modulated by the external perturbation. This light is then coupled to another fiber or the same fiber by either reflection or transmission. The outputs of these sensors can be linear or nonlinear, and these types of sensors can also be used as on-off switches.

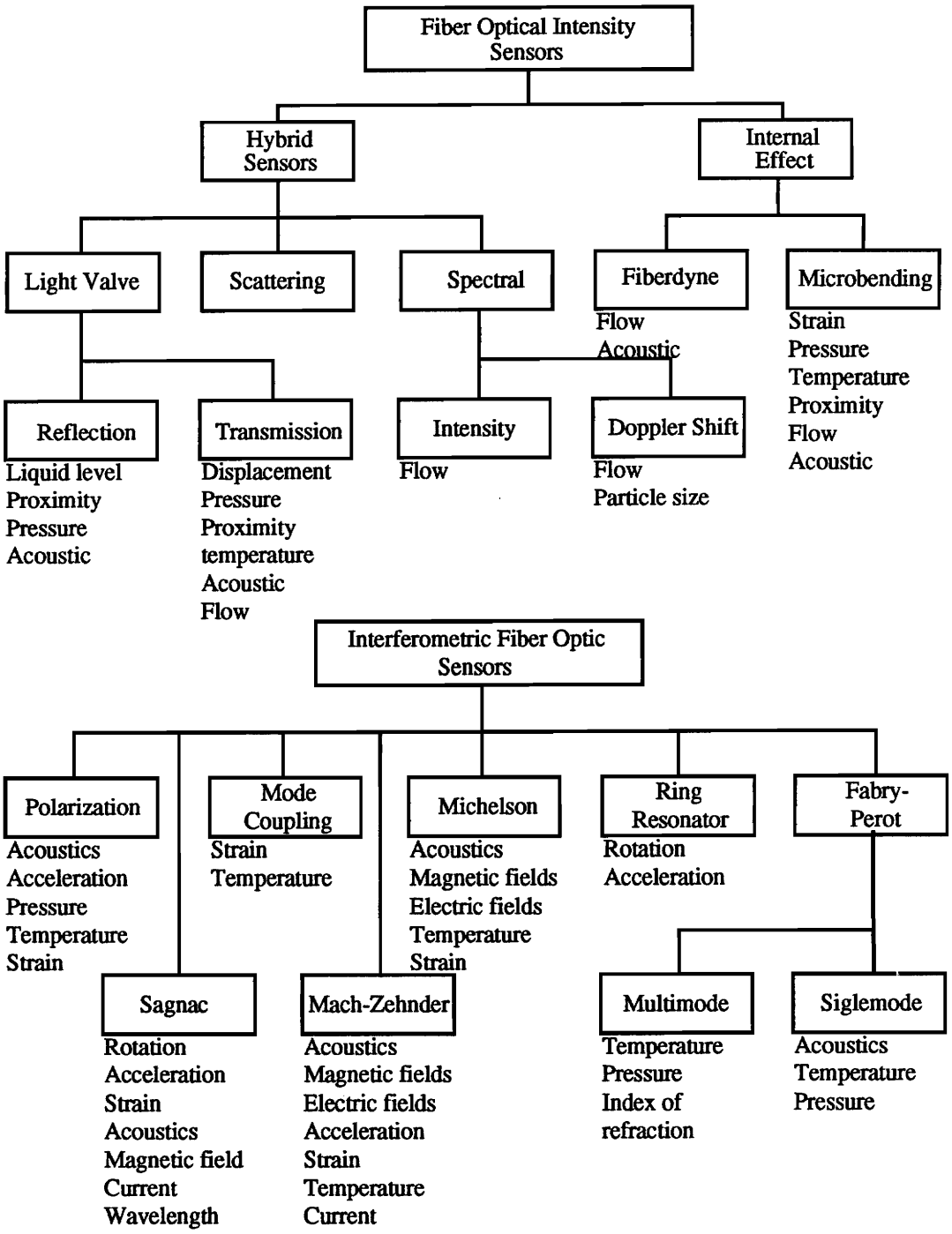

Figure 2.2. Classification of intensity based and interferometric fiber sensors [2.4,2.1].

Scattering light sensors often generate a frequency modulated optical intensity or an optical spectral shift, and the sensor accuracy is not very much affected by intensity fluctuations of the source. Doppler effect scattering sensors measure the Doppler frequency shift of the light scattered back from moving particles and thus, can be used for flow velocity measurements. On the other hand, spectral sensors configurations use optical emission from the object to be monitored. The simplest form of spectral sensor is the temperature sensor based on blackbody radiation of the heated fiber tip [2.6].

Optical intensity is modulated inside the fiber itself in the internal effect fiber intensity sensors. The two main classes of internal effect sensors are the microbending and the fiberdyne sensors. The optical power in a multimode fiber, redistributes among the various modes when the fiber is bent, twisted or perturbed. Modal filters can then used to measure this redistribution of power. This is known as the fiberdyne effect and has been used to develop a fluid flowmeter [2.7].

In microbending sensors the guided light in the core of the fiber is coupled into the cladding when the fiber is subjected a periodic microbending. If the cladding modes are prevented from coupling back to the core, the transmission loss of the guided light will be a function of the microbends [2.8].

2.2.2 Interferometric sensors

Phase modulated or interferometric sensors offer orders of magnitude increased sensitivity over intensity based sensors. The principle of interferometric sensors is the fringe pattern obtained when two coherent light beams, ideally from a single frequency source, interfere. The intensity of the interference signal is a function of the phase difference

between the two beams. The phase difference between the beams, in turn, is a function of the external perturbation and varies as the sine of the phase difference. In optical fibers the external perturbation causes a change in the refractive index of the core of the fiber or in its length.

A change in the refractive index or the length of the fiber affects the phase of the guided light. Thus, by isolating one beam (reference beam) from external perturbation, and subjecting the other beam (sensing beam) to perturbation, the intensity of the interference signal is a function of the perturbation. Hence, fiber optic interferometric sensors usually are comprised of two fibers: a reference fiber and a sensing fiber. The optical power through the fibers is combined by fiber optic couplers.

Fig 2.2(b) shows the different types of interferometric sensors. The four classical interferometers, the Mach-Zehnder, Michelson, Sagnac, and Fabry-Perot interferometers, have both bulk and fiber configurations. The fiber optic counterparts use directional couplers, mirrors, joints, polarizers, phase modulators and frequency shifters [2.9]. Two beam interferometry allows the measurement of extremely small differential phase shifts in the optical fiber generated by the measurand. Moss *et al* (1971) have determined periodic displacements of 10^{-14} m and the detectability is limited by the shot-noise of the photodetector [2.10].

Several techniques have been achieved for linearization of the transfer function of the interferometers. They are the (i) active homodyne, (ii) passive homodyne, and (iii) heterodyne techniques. In the active homodyne technique, a piezoelectric based fiber optic phase modulator is incorporated in the reference arm to maintain the sensor at the quadrature point or the point of maximum sensitivity. A servo system is then used to lock

the interferometer and the amplitude of the peak phase is obtained by band pass filtering at the signal frequency.

Interferometers can be configured to produce two outputs which vary as a quadrature function of the phase difference between the reference and the signal arm. The two signals are then filtered through a high pass filter and are combined to produce an output signal that is independent of signal fading [2.11]. Heterodyne and pseudo-heterodyne methods have a infinite phase tracking range and are free from signal fading problems. In this method the light in one of the arm of the interferometer is frequency shifted with respect to the other (done by a Bragg cell). The carrier is phase modulated by the signal which is demodulated at the output of the interferometer. The next section describes a very sensitive and geometrically versatile interferometric sensor.

2.3 Extrinsic Fabry-Perot Interferometer (EFPI)

Fiber optic Fabry-Perot (FP) sensors are very sensitive to temperature, mechanical vibration, acoustic waves, and magnetic fields [2.12]. Several techniques to fabricate a FP cavity exist. FP cavities have been created by Bragg gratings, air-glass interface for reflection and a pair of semi-reflective splices at locations in a continuous length of fiber. When air is the medium in the FP cavity, it is termed as extrinsic Fabry-Perot interferometer (EFPI), otherwise, it is termed as intrinsic Fabry-Perot interferometer (IFPI). The next subsections describe the construction of an EFPI and the theory of its operation.

2.3.1 Sensor construction

The main advantages of the extrinsic configuration over the intrinsic method are the avoidance of polarization problems and the detection of axial strain components. Fig. 2.3 shows the schematic of an EFPI and the setup for the operation of the interferometer. Light from a monochromatic source is launched into one arm of a bi-directional coupler while the other arm has a photodetector attached to it. The coupler is fabricated from an optical fiber that is singlemode at the wavelength of the light emitted by the source. The third arm of the coupler is used to fabricate the sensor. A low-finesse cavity is formed by the singlemode fiber that acts as the input/output fiber and a multimode fiber whose only purpose is to serve as a reflector [2.13]. The other end of the multimode fiber is shattered to prevent any reflections. The FP cavity formed by the endfaces of the singlemode and multimode fiber is placed a in hollow silica tube and the ends of the tube are glued to the fibers using epoxy. The distance between the two epoxied points is known as the gage length and the air gap between the endfaces of the singlemode and multimode fiber is called as the gap separation.

2.3.2 Theory of operation

The endfaces of the singlemode and the multimode fibers form glass/air and air/glass interface respectively. This results in Fresnel reflection from the two endfaces. The reflection R1 (reference reflection) from the singlemode endface and the reflection R2 (signal reflection) from the multimode endface interfere in the input/output fiber. Even though there are multiple reflections in the FP cavity, they are neglected because of the low-finesse.

External perturbation on the sensor causes the two fibers to move longitudinally with respect to each other. This displacement results in a change in the phase difference between the two signals, R1 and R2. The change in the phase difference modulates the intensity of

light through the input/output fiber. This variation in the intensity is monitored by the photodetector attached to the bi-directional coupler.

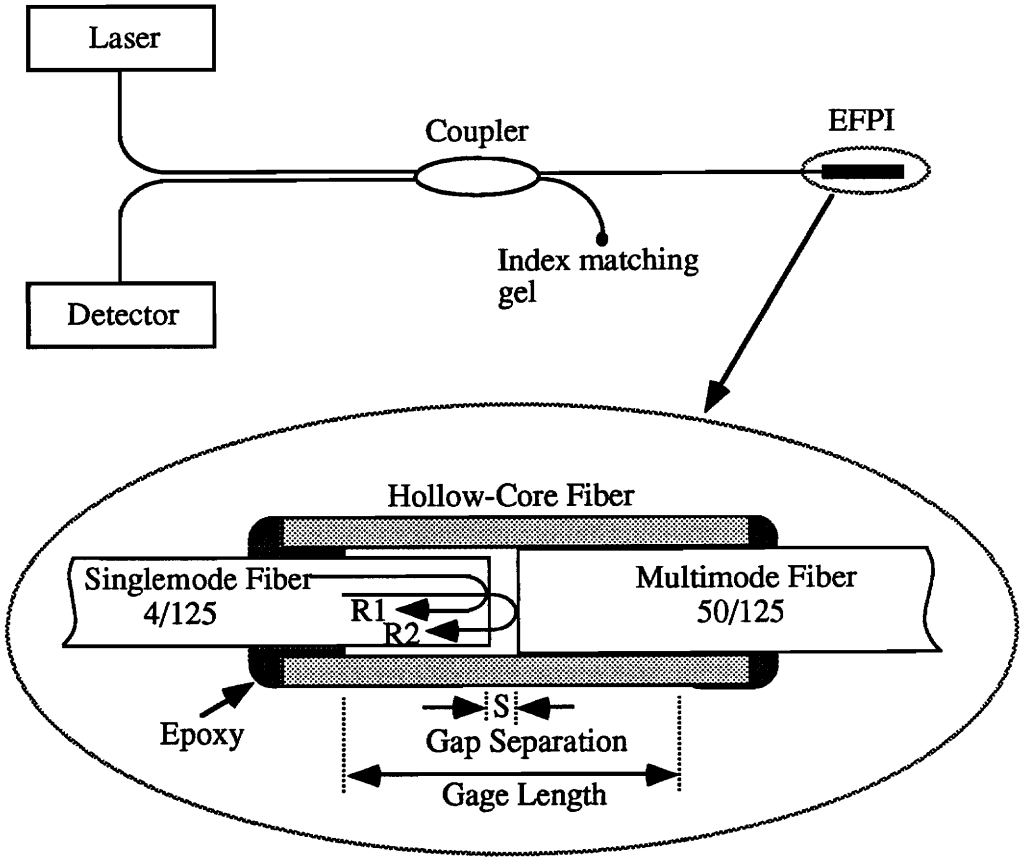

Figure 2.3. Schematic of an EFPI and the setup for the operation of the interferometer.

The coherent plane wave detected at the output of the sensor can be approximately represented in terms of its complex amplitude U_i (x, z, t), given by

$$U_i = A_i \exp(j\phi_i), \quad i = 1, 2, \tag{1}$$

where the variable A_i can be a function of the transverse coordinate x and the distance traveled z and the subscripts i = 1, 2 stand for the reference and sensing reflections

respectively. Assuming the reflection coefficient $A_1 = A$, the sensing reflection can be approximated by the relation

$$A_2 = A\left[\frac{ta}{a + 2s\tan\left(\sin^{-1}(NA)\right)}\right], \tag{2}$$

where a is the fiber core radius, t is the transmission coefficient of the air/glass interface (0.98), s is the air-gap separation, and NA is the numerical aperture of the singlemode fiber. The observed intensity at the detector is a superposition of the two amplitudes and is given by

$$I_{det} = \left|U_1 + U_2\right|^2 = A_1^2 + A_2^2 + 2A_1A_2\cos\left(\phi_1 - \phi_2\right), \tag{3a}$$

which can be rewritten as

$$I_{det} = A^2\left[1 + \frac{2ta}{a + 2s\tan\left(\sin^{-1}(NA)\right)}\cos\left(\frac{4\pi s}{\lambda}\right) + \left(\frac{ta}{a + 2s\tan\left(\sin^{-1}(NA)\right)}\right)^2\right], \tag{3b}$$

where we have assumed that $\phi_1 = 0$ and $\phi_2 = 4\pi s/\lambda$ and λ is the wavelength of operation in free space [2.13]. Fig. 2.4 shows the plot of intensity of the signal at the detector versus the air-gap separation of the EFPI.

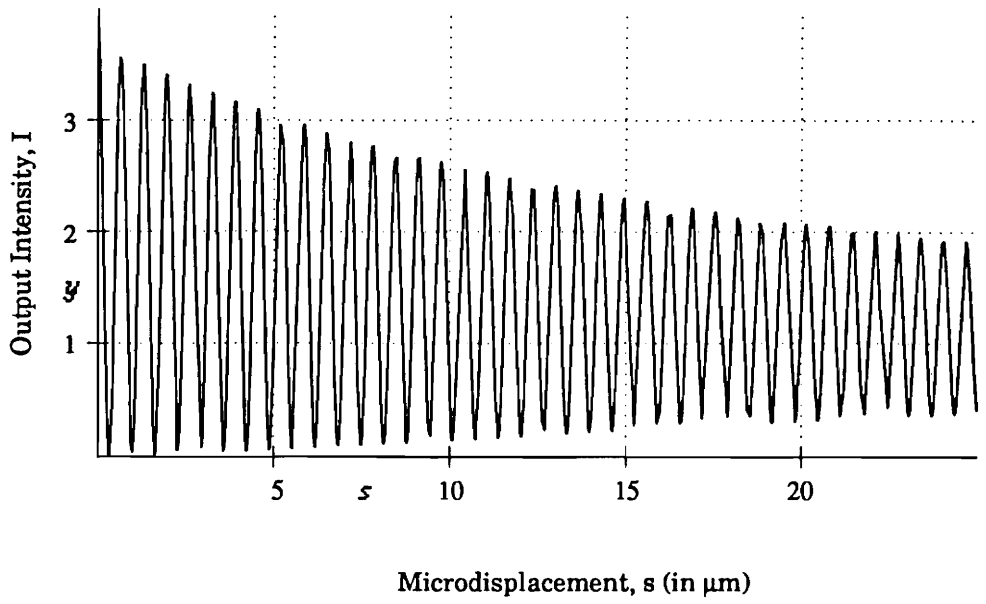

Figure 2.4. Plot of intensity of the signal at the detector versus the air-gap separation of the EFPI.

Chapter 3 - Surface acoustic wave detection

3.1 Introduction

It is well known that prior to structural failure, microfractures develop and propagate in the structure [3.1]. These microfractures release acoustic energy caused by the sudden localized changes in the stresses in the material [3.2]. The acoustic energy propagate to the surface of the structure and traverse along the surface of the specimen. These waves that travel along the surface of the structure are known as surface acoustic waves (SAW), or Rayleigh waves after Lord Rayleigh (John Strutt) who first discovered this phenomenon.

Monitoring acoustic emission (AE) events is essential for anticipating catastrophic structural failures. Surface acoustic waves produced by AE provide a way for evaluating the structure or material without damaging it. The advantage of using SAW over bulk waves produced inside the material is that it is a surface phenomenon, thus facilitating easier access, probing, and measurement. Also, the attenuation of SAW is very less compared to the attenuation of bulk waves, thus, sensor sensitivity requirements are not that severe.

Piezoelectric transducers (PZT) have been traditionally used to detect surface acoustic waves. However, current research has shown the feasibility of using optical fiber sensors for detection of acoustic/ultrasonic pulses. An optical fiber-based acoustic ultrasonic stress wave sensor has been demonstrated [3.3]. Optical fiber sensors provide higher sensitivity, immunity to electromagnetic radiation, higher operating temperatures and no resonant frequencies as compared to a PZT.

Particle motion associated with SAW exhibits elliptical retrogate paths and can be decomposed into two orthogonal components. One component moves in the direction of the wave and parallel to the surface of the structure and the other moves normal to the surface. SAW frequencies usually range from 20 kHz to 2 MHz with amplitude levels in the sub-angstroms range. The next section describes a non-contact optical fiber-based interferometric technique for measuring the absolute amplitudes of SAW.

3.2 Absolute SAW amplitude measurement using a hybrid interferometer

Interferometric sensors depend on the path length difference between the reference and sensing signals, and are thus more sensitive than other fiber sensors. This section describes a hybrid interferometer incorporating secondary phase modulation for measuring absolute SAW amplitudes. The interferometer uses a PZT cylinder to modulate the SAW signal induced on the specimen under test.

3.2.1 Hybrid interferometer

The hybrid interferometer comprises the combination of a classical Michelson and a Mach-Zehnder interferometer. Fig. 3.1 shows the experimental arrangement of the hybrid interferometer. Light from a Helium-Neon laser operating at 633 nm is split by a bulk optic beam splitter after passing through a collimator. The beam splitter is coated with anti-reflection coating to avoid back reflection into the laser. One of the two beams is launched into one input of a 3 dB, 2X2 coupler that is fabricated from a singlemode fiber with a cutoff wavelength of 633 nm. This arm is referred to as the reference arm. The other beam from the beam splitter is reflected from the specimen on which the SAW is launched. This reflection, after passing through the beam splitter, is launched into the second input port of the coupler. This arm is referred to as the sensing arm. One of the input arms of the coupler is wound round a piezoelectric transducer cylinder.

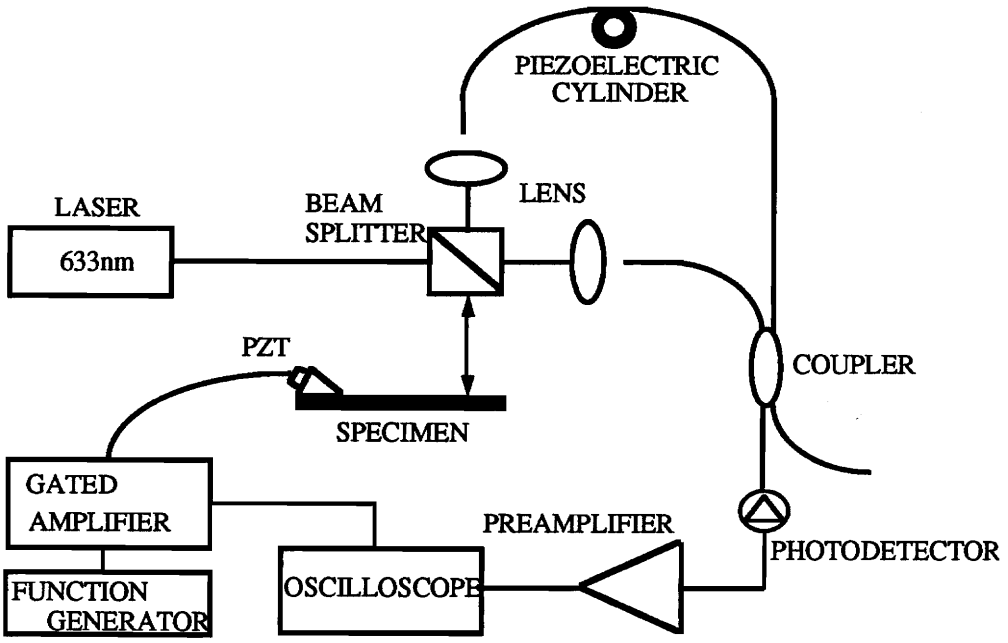

Figure 3.1. Experimental setup of the hybrid interferometer.

The interference between the light guided in the sensing and the reference arm is monitored at one of the output ports of the coupler using an avalanche photodiode (APD). The interference signal detected by the APD is amplified by a broadband amplifier and observed on the oscilloscope. Acoustic emission signals are simulated on the material using a PZT mounted on wedge at an angle of 30° driven by a gated amplifier. A function generator is used to provide the input signal to the gated amplifier. The signals are triggered by the gated amplifier.

3.2.2 Calibration of the PZT modulator

Two beam interferometry is extensively used for measuring small differential phase shifts caused by the perturbation being measured. The optical phase delay (in radians) of the light guided through a fiber is given by

$$\phi = nkL, \tag{3.1}$$

where n is the refractive index of the core of the fiber, k is the wave number ($2\pi/\lambda$, λ being the wavelength), and L the physical length of the fiber. Small variations in phase can be expressed as

$$\frac{d\phi}{\phi} = \frac{dL}{L} + \frac{dn}{n} + \frac{dk}{k}. \tag{3.2}$$

Thus phase can be changed by changing the physical length of the fiber. The PZT cylinder is used to change the phase of the signal through one arm of the interferometer. The

intensity of the output interference signal at one of the output ports of the coupler is then given by

$$I = I_1 + I_2 + 2\sqrt{I_1 I_2}\cos(\phi_r - \phi_s), \tag{3.3}$$

where I_1 and I_2 are the intensities of the light guided through the reference arm, and the sensing arm, and ϕ_r and ϕ_s are the phases of the reference arm and the sensing arm. The differential phase shift $\Delta\phi = \phi_r - \phi_s$ in the interferometer is separated into a signal term of amplitude ϕ_s and angular frequency ω_s and a slowly varying phase shift ϕ_d. The output of the interferometer can then be written as

$$I = I_1 + I_2 + 2\sqrt{I_1 I_2}\cos(\phi_d + \phi_s \sin\omega_s t). \tag{3.4}$$

Several techniques exist for retrieving the signal information in the presence of a slowly varying phase drift. They can be broadly classified as active homodyne, passive homodyne and heterodyne detection [3.4]. Active homodyne technique requires a PZT feedback mechanism to stabilize the interferometer. Heterodyne detection requires an optical frequency shifter and therefore is more complex to implement.

A number of demodulation schemes exist in the passive homodyne detection technique. These include the J_0(null), J_1(max), J_1(null), J_1/J_2, and the J1..J4 technique [3.5]. The J1..J4 technique allows direct linear readout of the dynamic phase shifts in a no feedback, no phase bias interferometer. The instantaneous voltage at the APD can be written in terms of Bessel function $J_n(x)$ of the first kind [3.5]:

$$V(t) = A + B\left(\begin{array}{l}\left\{J_0(\phi_s) + 2\sum_{n=1}^{\infty} J_{2n}(\phi_s)\cos(2n\omega_s t)\right\}\cos(\phi_0(t)) - \\ \left\{2\sum_{n=1}^{\infty} J_{2n-1}(\phi_s)\sin[(2n-1)\omega_s t]\right\}\sin(\phi_0(t))\end{array}\right), \quad (3.5)$$

where A = 2v and B = 2vb (with v being the voltage due to either of the fiber outputs and b the interferometer mixing efficiency), ϕ_S is the modulation depth and $\phi_O(t)$ is the random phase shift due to ambient temperature and pressure variations. Using the recurrence relation between Bessel functions of the first kind,

$$x = \frac{2iJ_i(x)}{J_{i-1}(x) + J_{i+1}(x)}, \quad (3.6)$$

x can be determined without any phase bias as

$$x^2 = \frac{4i(i+1)V_iV_{i+1}}{(V_i + V_{i+2})(V_{i-1} + V_{i+1})}, \quad (3.7)$$

where $i > 1$, V_i is the voltage amplitude of the ith frequency component. When i = 2, the phase strength is given by

$$\phi_s = \sqrt{\frac{24V_2V_3}{(V_1 + V_3)(V_2 + V_4)}}. \quad (3.8)$$

By passing the output of the interferometer through a spectrum analyzer, the amplitude of the phase signal can be obtained unambiguously. Since $\sin(\phi_O(t))$ and $\cos(\phi_O(t))$ do not appear in Equation 3.8, it implies that random phase drifts, polarization drifts, fringe

contrast variations and intensity fluctuations of the laser do not affect the readout of the phase amplitude.

For measuring the phase shift produced by the interferometer, the PZT cylinder was driven by a sinusoidal signal at 800 kHz using a function generator. The interferometer was operated without the SAW signals. The drive voltage to the PZT cylinder was varied and the phase shift was measured using Equation 3.4. Fig. 3.2 shows a typical time domain and frequency domain plot of the interferometer. Fig. 3.3 shows a plot of the measured phase shift versus the drive voltage (calibration curve) to the PZT cylinder for two independent trials. Phase shift coefficients (PSC) of 2.3 radians/volt were measured.

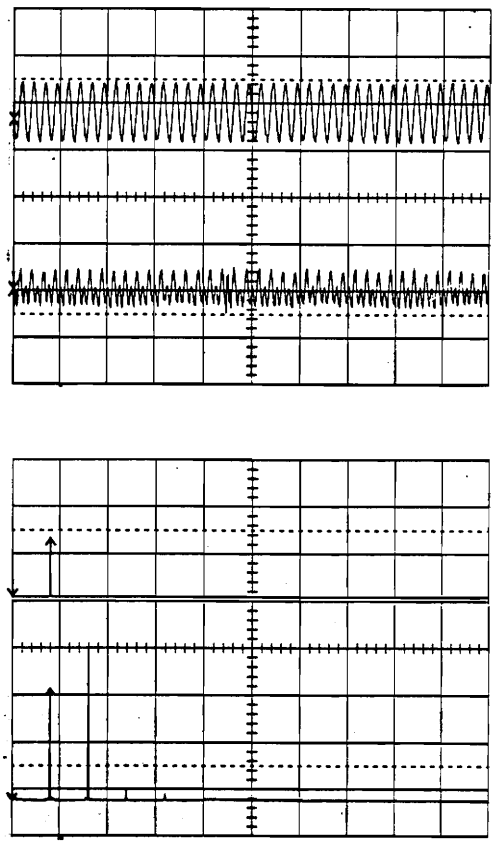

Figure 3.2. A typical time domain and frequency domain plot of the output of the interferometer when the PZT cylinder is driven by a sinusoidal input.

In the next, step the drive voltage on the PZT cylinder was set corresponding to a phase shift of 0.1 radians. The acoustic pulses were induced into an aluminum specimen using a PZT driven by the gated amplifier.

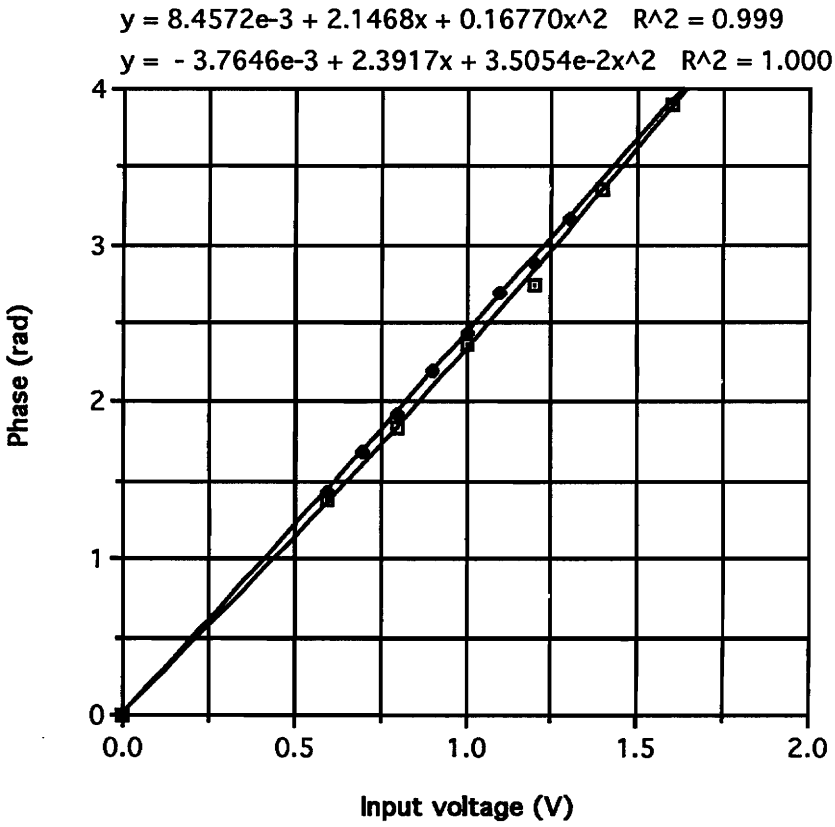

Figure 3.3. Calibration curve of the PZT cylinder.

3.2.3 Demodulation of the SAW signal

The PZT mounted on the wedge was driven by ultrasonic pulses from the gated amplifier at a frequency of 1.2 MHz to induce SAW on the aluminum specimen. The phase due to the SAW signal is modulated by the phase due to PZT modulator. The instantaneous voltage at the photodetector can now be written as

$$V(t) = A + B\cos\left(\phi_c(t) + \phi_s(t) + \phi_o(t)\right), \tag{3.9}$$

where A = 2v and B 2vb (with v being the voltage due to either of the two fiber outputs and b is the fringe visibility), $\phi_C(t) = L\cos(\omega_C t)$, L is the modulation depth and ω_C is the angular frequency of the carrier, $\phi_S(t) = M\cos(\omega_S t)$, M is the modulation depth and ω_S is the angular frequency of the SAW signal and $\phi_O(t)$ is the random phase drift. Bessel functions $J_n(x)$ of the first kind can be used to expand Equation 3.9.

The expansion combined with recurrence relation for J_n can be used to determine the phase shift due to the SAW signal as

$$M = 2\left(\frac{V_s}{V_c}\right)\left(\frac{J_1(L)}{J_0(L)}\right), \tag{3.10}$$

where V_C and V_S are the voltage amplitudes of the carrier and the SAW signal respectively. All the random phase drift factors associated with the source, the interferometer, and the detector circuitry are eliminated by cancellation of common factors in the voltage amplitudes. This expression utilizes an approximation of the Bessel function magnitude for low values of argument (phase shift) in contrast to the J0.J2 technique [3.6]. The drive voltage is varied on the PZT and the phase shift is measured from Equation 3.10. Fig. 3.4 shows a typical time domain and frequency domain plots of the output of the interferometer. Fig. 3.5 shows the plot of the phase shift generated by the SAW versus the drive voltage to the PZT producing the SAW, for three independent trials. Phase shifts of 10-30 milliradians were measured.

The phase shift in a Michelson interferometer is given by

$$\Delta\phi = \frac{2\pi(\text{path difference})}{\lambda}, \tag{3.11}$$

where λ is the wavelength (633 nm) of the source. The SAW amplitude is then given by A = path difference / 2. Fig. 3.6 shows the plot of the SAW amplitude versus PZT drive voltage. SAW amplitudes in the range 5- 15 angstroms were measured. The detection of such low amplitude signal requires the inclusion of a broadband preamplifier.

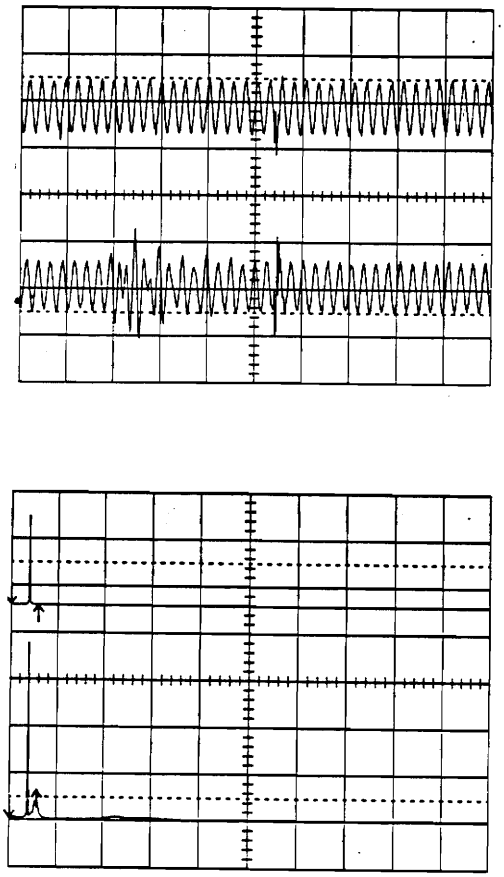

Figure 3.4. A typical time and frequency domain plot of the output of the interferometer with the SAW signal modulated over the PZT cylinder signal.

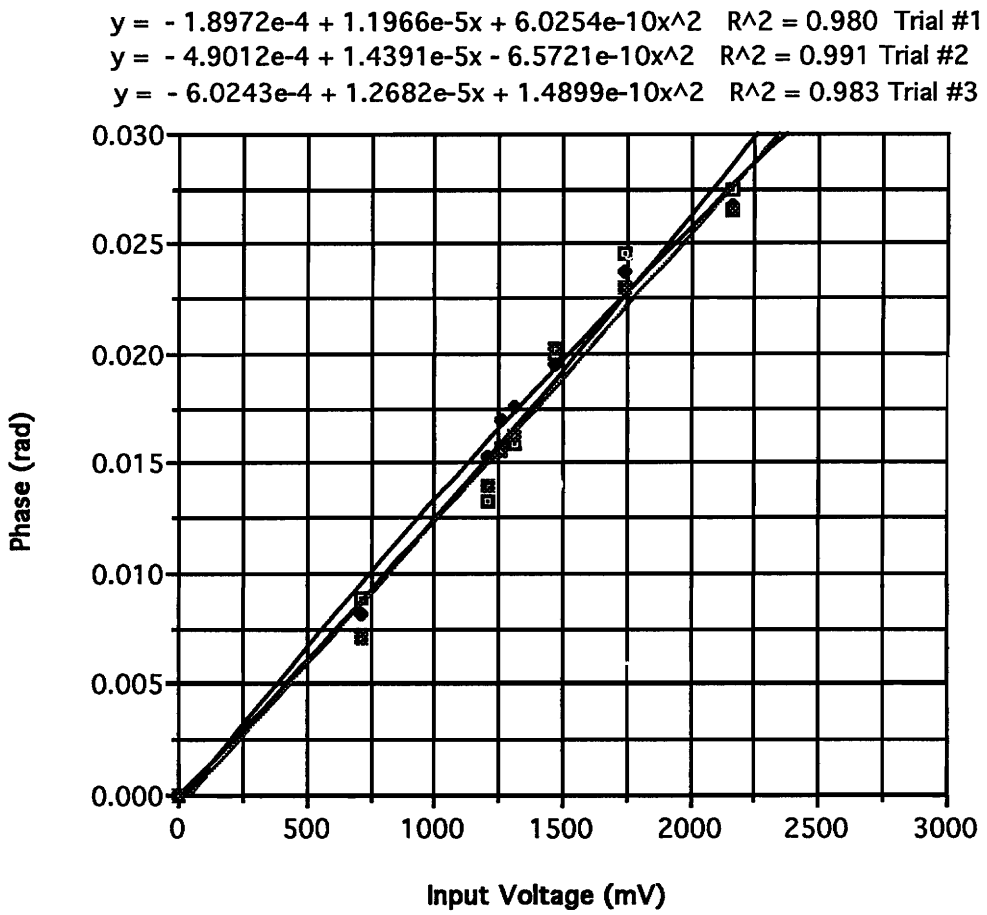

Figure 3.5. A plot of the phase shift generated by the SAW versus the drive voltage to the drive voltage to the PZT.

3.3 Broadband preamplifier design

The minimum detectable surface acoustic wave amplitude is limited by the signal to noise ratio of the complete fiber optic system comprising the laser and its drive electronics, the sensor (EFPI sensor), the photodetector and the detection electronics. Detection of low amplitude SAW signals can be achieved by minimizing the sources of noise. Generally in a fiber optic sensor system, the noises can arise from the laser, the detector and preamplifier electronic noise. Mentioned below are the major sources of noises in an EFPI fiber optic system.

Laser noise : Laser noise can be classified into source intensity fluctuations and wavelength fluctuations. For an optical interferometer such as an EFPI fiber sensor, wavelength fluctuations give rise to a noise called the phase noise. Source intensity fluctuations and phase noise are usually caused by a number of factors, such as the spontaneous emission and electron-hole recombination, back reflection and mode jumping.

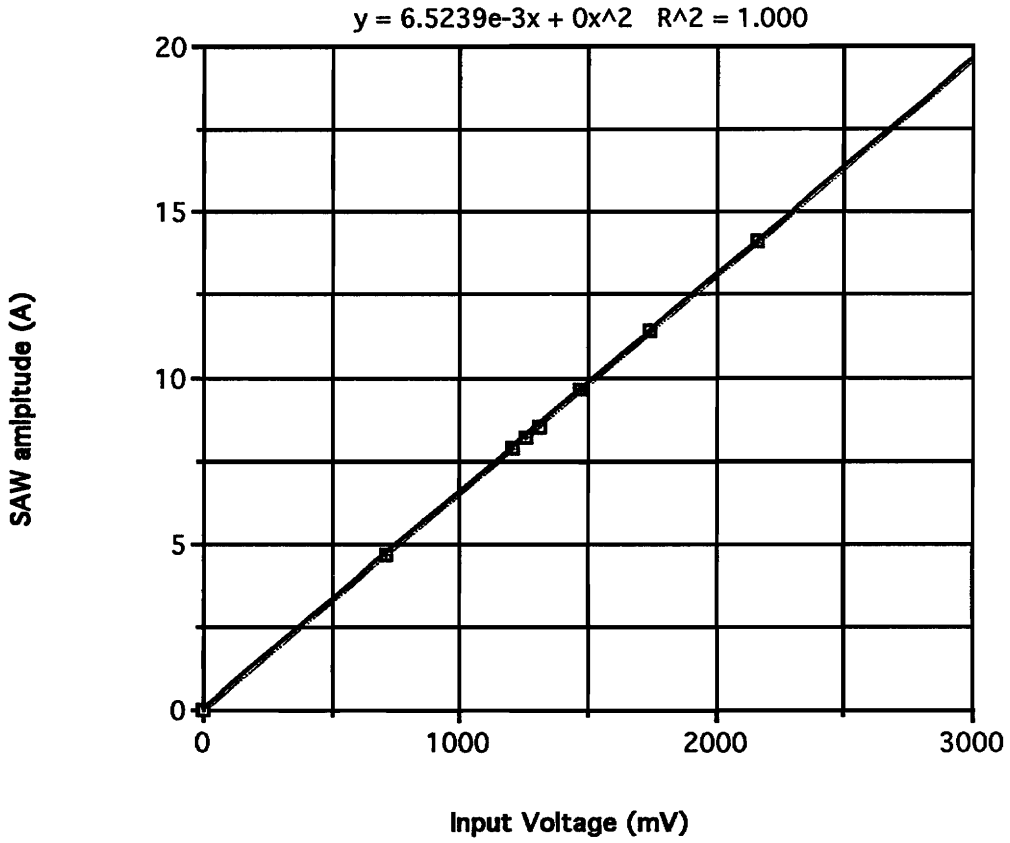

Figure 3.6. A plot of the SAW amplitude versus PZT drive voltage.

Electronic noise : Electronic noise can be classified into thermal noise, shot noise, dark noise and flicker or 1/f noise. While thermal, shot and dark noises are white noises (Gaussian in nature) flicker noise is not a white noise.

Thermal noise : In any resistive material, such as a resistor or a piece of semiconductor, the average kinetic energy possessed by the electrons and holes, or the free charge carriers, is equal to KT, where K is the Boltzman's constant equal to 1.38 X 10^{-23} J/K and T is the absolute temperature in Kelvin. These moving charges even in the absence of an electric field, generate an electric current whose mean value is zero, thus producing a fluctuating voltage across the material. Thermal noise in a PIN photodiode manifests itself as a mean square current noise given by

$$\overline{i_t^2} = \frac{4KTB}{R}, \tag{3.13}$$

where R is the load resistance across the photodiode and B is the bandwidth.

Shot noise : In a PIN photodiode the current produced when an optical power is incident on it is statistical in nature, in that there is a fluctuation in the number of charge carriers. Schottky showed that the noise current known as shot noise has a mean square value given by

$$\overline{i_s^2} = 2eBI_p, \tag{3.14}$$

where I_p is the average photocurrent and e is the electronic charge.

Dark noise : The photodiode dark current is the current that flows due to the thermally generated electrons and holes in the pn junction of the photodiode. The mean square value of the dark current is given by

$$\overline{i_d^2} = 2eBI_d, \tag{3.15}$$

where I_d is the dark current in the photodiode.

Flicker or 1/f noise : Flicker noise manifests itself as variations in electrical conductance and is inversely proportional to the frequency, and is thus dominant in semiconductors at low frequencies. This has been attributed to the rate of thermal generation of charge carriers.

In the fiber sensor system, the variation of the optical power level at the detector is monitored using a direct detection scheme. The signal to noise ratio of the system at the detector after combining the noise sources is given by

$$\frac{S}{N} = \frac{I_p^2}{2eB\left(I_p + I_d\right) + \frac{4KTB}{R_L} + \overline{i_{amp}^2}}. \qquad (3.16)$$

To obtain high bandwidths, the capacitance's due to the detector and the amplifier are to be minimized. The reciprocal of the time constant must be greater than, or equal to, the post detection bandwidth B;

$$\frac{1}{2\pi R_L C_T} \geq B, \qquad (3.17)$$

where R_L is the load resistance across the detector and C_T is the total capacitance. Assuming the capacitance's are minimized, the other parameter which affects B is the load resistance. To increase B it is necessary to reduce R_L which, in turn, introduces a thermal noise penalty. A trade-off therefore exists between the maximum bandwidth and the level of thermal noise which may be tolerated.

Three basic amplifier configurations are frequently used in optical fiber communication receivers. The simplest and the most common of them is the voltage amplifier that uses an

effective input resistance. The second configuration consists of a high input impedance amplifier together with a large detector bias in order to reduce the effect of thermal noise. However, this configuration tends to degrade the frequency response. The third configuration overcomes the drawbacks of the high input impedance amplifier with negative feedback. The device therefore operates as a current mode amplifier (transimpedance amplifier).

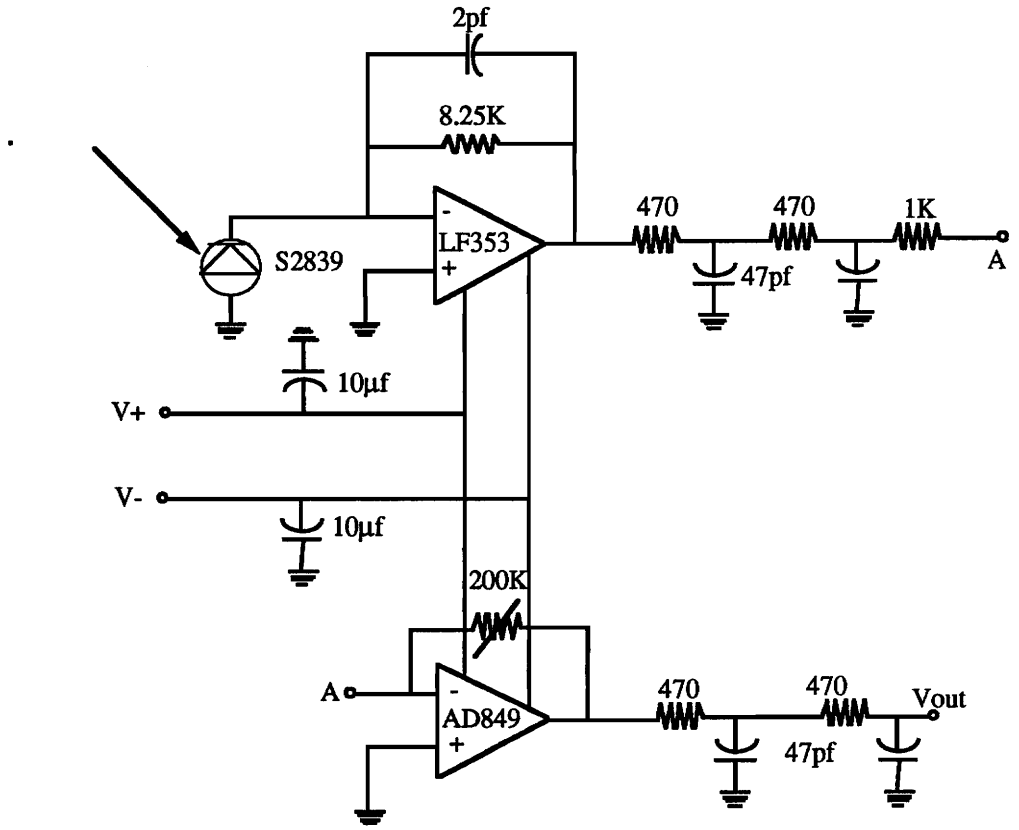

Figure 3.7. Circuit diagram for the preamplifier system.

Fig. 3.7 shows the circuit diagram for the preamplifier system. The circuit is comprised of two stages, a transimpedance stage and a gain stage. The transimpedance stage uses a low noise operational amplifier (LF353) with a feedback resistance of 8.21 KΩ and a feedback capacitance of 2 µF. The feedback capacitor is used to remove the effect of "gain peeking"

usually observed in transimpedance amplifiers. The transimpedance stage has been optimized for maximum gain while ensuring minimum noise for a 3 dB bandwidth of 1.5 MHz. 10 μF capacitors were used to decouple the power supply leads connected to the chips.

The transimpedance stage is followed by two stages of a passive RC low-pass filter with a 3 dB bandwidth of 2 MHz to reduce the noise. The second stage is a voltage amplification stage with a gain of 200, making use of a high bandwidth operational amplifier AD849 (720 MHz unity gain bandwidth). Two stages of the RC filter similar to the ones used before the second stage were added to further decrease the noise. The decoupling capacitors, the photodiode, and the resistors were placed close to the chip leads to avoid stray capacitance's. The sensitivity of the system was measured to be 0.86 V/μW and the noise floor, when shielded from external radiation, was observed to be 18 mV. The signal to noise ratio for the system was measured to be 57 dB

3.3.1 Theoretical minimum detectable gap change of an EFPI sensor

The output of an EFPI is given by Equation 3.3. The first two terms constitute the dc component and the third term constitutes the ac component. If P_0 is the power entering the EFPI then the maximum power seen at the detector end due to the reflections is approximately $0.04P_0$ (4% Fresnel reflection at glass/air interface) for small air gaps considering 3 dB loss of the 2x2 coupler. When the sensor is operated at the Q-point, the optical power becomes $0.02P_0$. This static optical power produces a dc current at the photodetector given by,

$$I_{dc} = \alpha(0.02P_o), \tag{3.18}$$

where α is the responsivity of the photodetector. This current causes an rms. shot noise given by

$$i_{noise} = \sqrt{2eBI_{dc}} = \sqrt{0.04\alpha eBP_o}, \tag{3.19}$$

where e is the electronic charge and B is the bandwidth of the preamplifier system. If the acoustic wave is sinusoidal, then the rms air gap difference $\Delta L/(2)^{1/2}$ gives an rms signal current given by [3.7]

$$i_{sig} = \alpha P_{sig} = \frac{2\alpha(0.02P_o)\Delta L}{\lambda\sqrt{2}}, \tag{3.20}$$

where λ is the wavelength of the source. Equating signal and noise currents to determine the minimum optical path change between the endface reflections we get

$$\Delta L = \lambda\sqrt{\frac{eB}{0.02\alpha P_o}}, \tag{3.21}$$

substituting λ = 830 nm, B = 1.5 MHz, α = 0.5 A/W and for an input power of 1 mW we get the minimum detectable path difference, ΔL = 1.28 A°.

3.3.2 Practical minimum detectable optical path change

An EFPI sensor was fabricated with a gage length of 1 cm and a gap separation of 20 μm. The peak to peak noise floor measured out of the preamplifier was 40 mV with the laser

An EFPI sensor was fabricated with a gage length of 1 cm and a gap separation of 20 μm. The peak to peak noise floor measured out of the preamplifier was 40 mV with the laser switched on. The sensor was strained so that it passed through several fringes. Fig. 3.8 shows the output from the optical preamplifier due to the straining of the EFPI sensor.

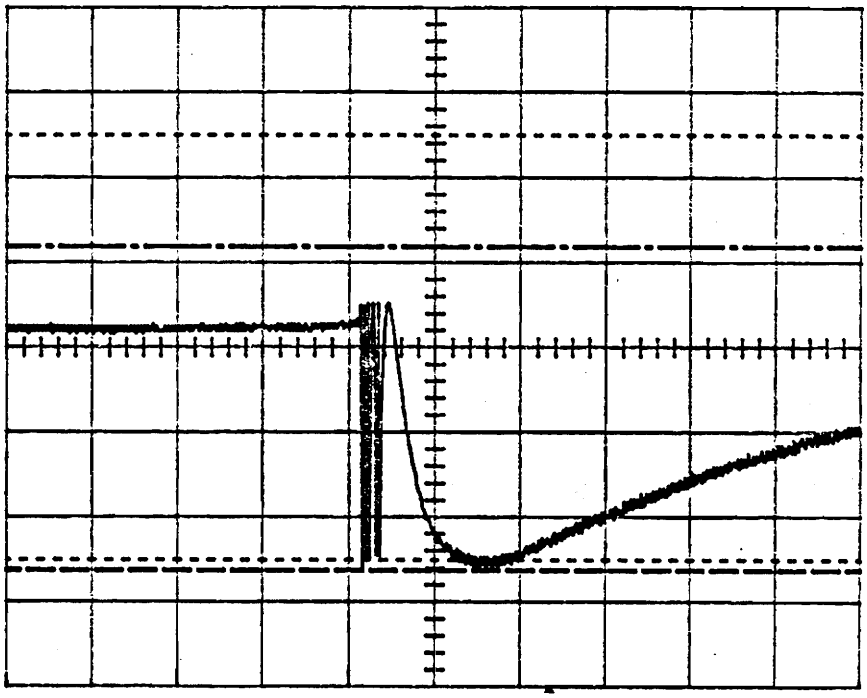

Figure 3.8. Output of an EFPI sensor.

For calculating the practical minimum detectable air gap change, various points on the waveform are marked on a theoretical curve in Fig. 3.9. Referring to the plot, the signal can be represented by

$$V = V_o + \frac{(V_2 - V_1)}{2}\sin(\phi + \phi_0) = \frac{(V_2 + V_1)}{2} + \frac{(V_2 - V_1)}{2}\sin(\phi + \phi_0), \quad (3.21)$$

where ϕ_0 corresponds to the phase at the operating point of the sensor and V_1 and V_2 are the voltages as shown in Fig 3.9. Taking the derivative of the above equation and rearranging we get

$$d\phi = \left(\frac{2}{V_2 - V_1}\right)\left(\frac{dV}{\cos(\phi + \phi_o)}\right). \tag{3.22}$$

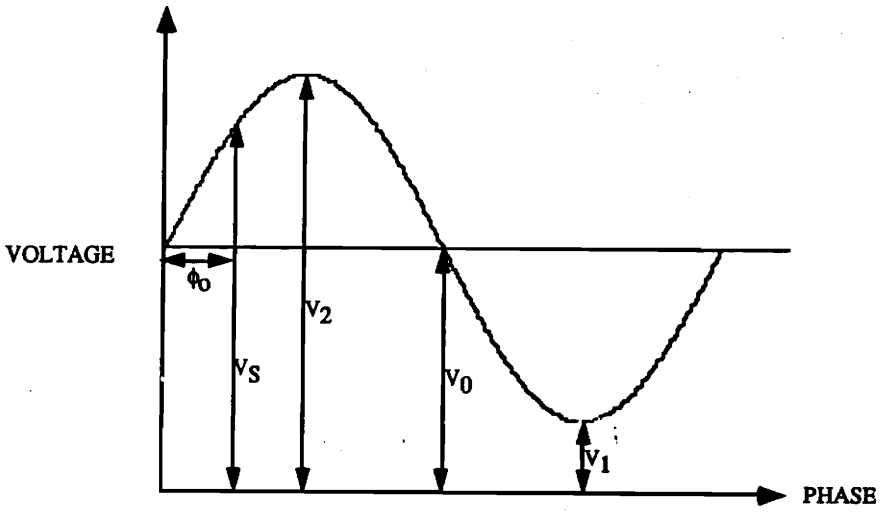

Figure 3.9. Theoretical curve for calculation of minimum detectable air gap change of an EFPI sensor.

If S is the gap separation of the two endfaces of the EFPI sensor then we infer that

$$d\phi = \frac{4\pi\, dS}{\lambda}, \tag{3.23}$$

where dS corresponds to the dynamic gap variation due to random noise. Substituting Equation 3.23 in Equation 3.22 and rearranging we obtain

$$dS = \left(\frac{2}{V_2 - V_1}\right)\left(\frac{\lambda}{4\pi}\right)\left(\frac{dV}{\cos(\phi + \phi_o)}\right), \tag{3.24}$$

It was observed that V2 = 2 V, V1 = 0.34 V and substituting λ = 830 nm, dV = 40 mV and calculating ϕ_O = 0.91 rad (observing V=0.51 V), we obtain practical dS = 58.4 A°. If the sensor is operated at the Q point then the minimum detectable gap change becomes 35.4 A°. Recall that this is based on the bandwidth of approximately 1.5 MHz, so the minimum detectable signal amplitude per root Hertz is approximately 0.003 A°.

Chapter 4 - Experimental arrangements, results and discussion

Material property determination by nondestructive means is increasing especially for in-process and in-service inspection of structural and electronic materials and components. Fiber optic sensors are proving to be a viable option for detecting imperfections in materials and structures [4.1, 4.2, 4.3]. This chapter describes the experimental setups and discusses the obtained results of pencil lead break tests, speed and attenuation measurement, and directional sensitivity of the EFPI sensor for material evaluation.

4.1 Pencil lead break tests

Several methods exist for simulating acoustic emission in materials. The most commonly used method to generate acoustic waves in materials is the Pentel pencil lead break. This is usually done by breaking a 0.3 mm diameter 2H material lead at an angle of 30° to the surface of the specimen on which the acoustic emission is being simulated. Fracture of a pencil lead causes a monopolar event which takes place as the load on the surface is

released [4.3]. Pencil lead fracture tests can be made repeatable by using jigs which ensure that a constant length of lead and angle is maintained [4.4].

An extrinsic Fabry-Perot interferometric sensor was fabricated for use in the pencil lead break tests. The EFPI was attached to the surface of a composite specimen (31 cm X 9.5 cm X 0.62 cm graphite bismalliumuth panel) using glycerin as the couplant. To maintain the sensor at the Q-point a piece of masking tape was attached to the multimode end of the sensor and strained until the Q-point was attained. Initially several trials of pencil lead fracture were performed with a 2 mm diameter lead of length 4 mm. The data was captured on the scope by triggering the signals with a default threshold voltage. Fig. 4.1 shows the experimental arrangement for the pencil lead break tests. It was observed that low frequencies dominated the signal detected by the lead fracture. Major components were found to be around 400 Hz and 20 kHz, which could be due to the contribution of the low frequency flexural waves and the vibration modes of the composite specimen.

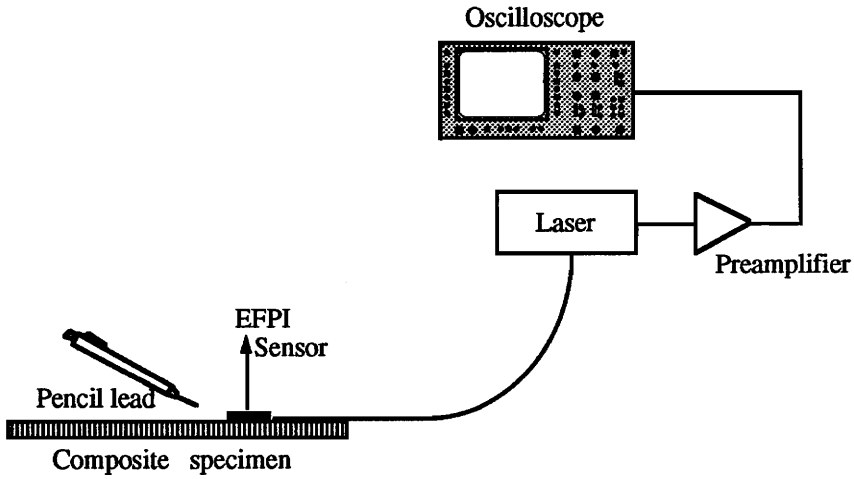

Figure 4.1. Experimental arrangement for the pencil lead break tests.

Pencil leads of diameters 0.5 mm and length 5 mm were broken about 2 cms away from the sensor along its longitudinal axis. It was observed after several trials that a frequency centered around 20 kHz was a significant contributor to the acoustic signal. However, higher frequency signals were not observed even when a Fourier transform was performed on selective sections of the time domain signal. This was attributed to the presence of the masking tape on the multimode fiber end of the sensor.

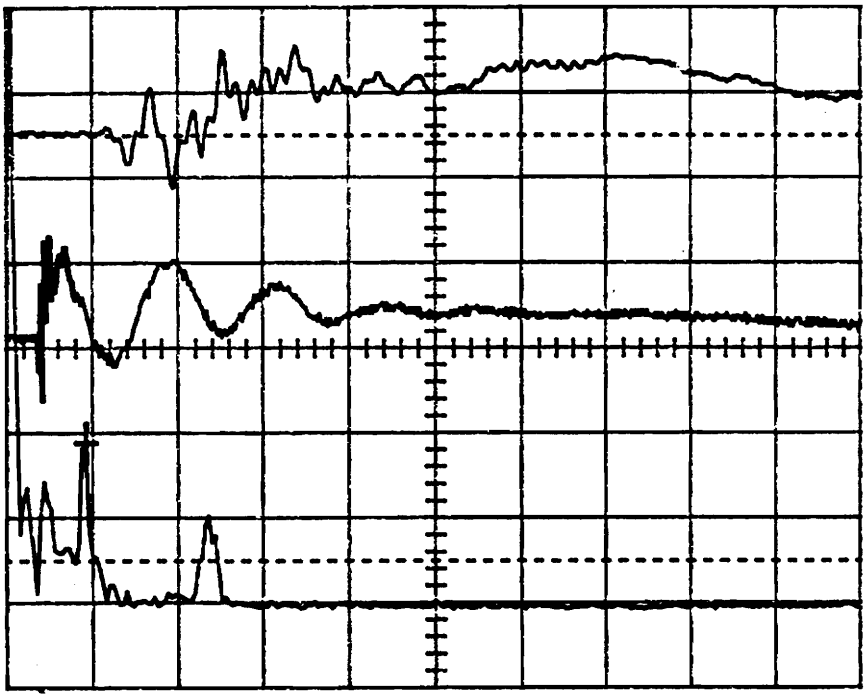

Figure 4.2. Typical time and frequency domain plot due to a pencil lead fracture.

After removing the masking tape several pencil leads were fractured in the vicinity of the sensor. The acoustic emissions from the fracture were observed on the oscilloscope. Fig. 4.2 shows a typical time and frequency domain plot of the signal detected due to the fracture. The major contributions for the detected acoustic signal were centered around 220 kHz and 400 kHz. To further quantify the acoustic signals 0.7 mm and 0.5 mm pencil

leads of lengths 3 mm were fractured at an angle of 30° to the surface of the composite specimen at about 1 cm away from the sensor along the longitudinal axis of the sensor. Fourier transforms were performed on the obtained signals and all the frequency peaks above a threshold of 5 mV were noted for ten pencil lead breaks. Figure 4.3a and 4.3b shows the data obtained for 0.7 mm and 0.5 mm lead fractures respectively. It can be seen from the plots that the major contributions of the signal are centered around 20 kHz, 240 kHz and 440 kHz. It was observed that there were no significant differences in the frequency components for the 0.7 and 0.5 mm pencil lead fractures. However, the average magnitude of the signals at each frequency is larger for 0.7 mm pencil lead breaks than that for 0.5 mm pencil lead breaks.

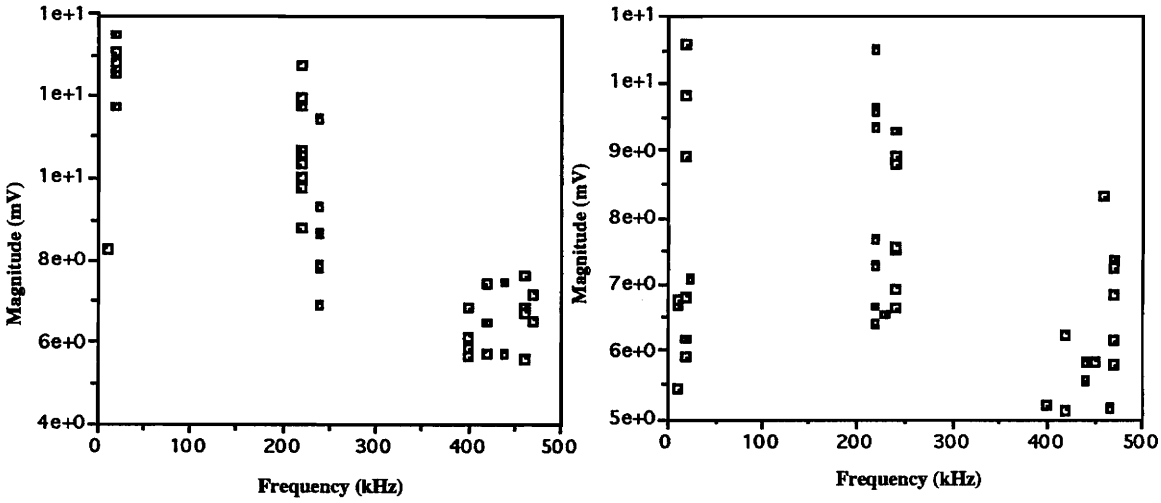

Figure 4.3. (a) Frequency plot for 0.7 mm pencil lead fracture. (b) Frequency plot for 0.5 mm pencil lead fracture.

4.2 Speed and attenuation measurements

Ultrasonic velocity is known to be a good measure of crystallographic texture. Precipitates, flaws, alternate phases affect the ultrasonic velocity. For instance, cast iron is

an alloy like steel but with a huge excess of carbon precipitated as graphite [4.5]. The morphology of graphite is the principle source of velocity variations in cast iron. The morphology varies from large thin flakes to tight little spheres. Thus, the shape of the graphite is one of the factors that determines the strength of the iron. Conversely, the strength of a material can be determined by measuring the velocity and attenuation of ultrasonic waves in the material.

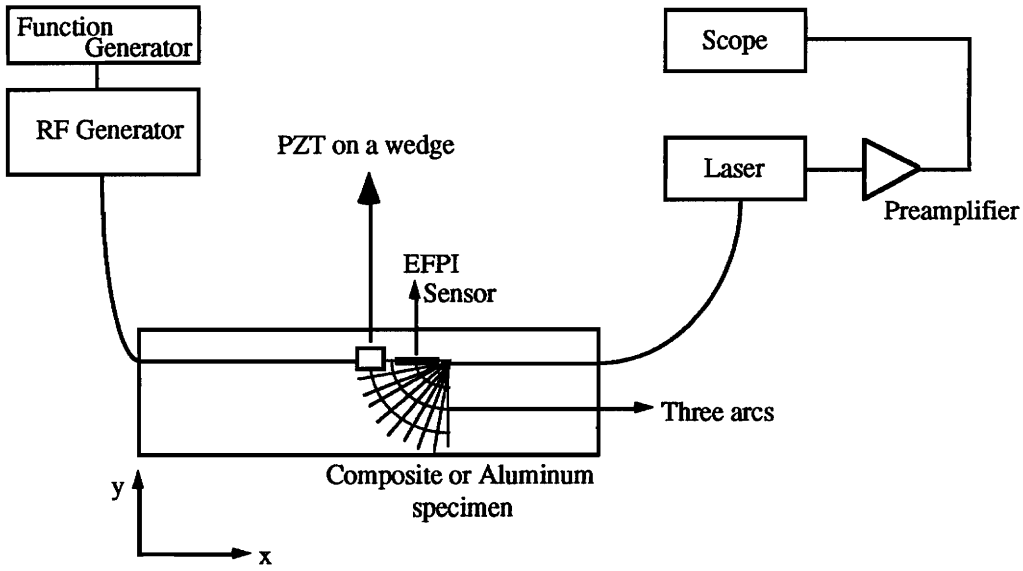

Figure 4.4. Experimental setup for measuring the speed and attenuation.

Fig. 4.4 shows the experimental setup for measuring the speed and attenuation of ultrasonic pulses in aluminum (31 inches X 48 inches X 0.2 inches) and composite (31 cm X 9.5 cm X 0.62 cm) specimens. Ultrasonic pulses at a frequency of 1.2 MHz are induced into the specimen under test by a PZT driven by a gated amplifier. An EFPI sensor is placed on the specimen to detect the acoustic signals. Glycerin was used as the couplant to couple the acoustic energy to the sensor.

The speed was calculated by measuring the time difference between the arrival times of two acoustic waves when the source was placed at two locations separated by a known distance. The same procedure was repeated on the composite panel. Fig. 4.5 shows the response of the EFPI sensor when it is interrogated with an SAW input pulse (1.2 MHz) at two different locations along the axis of the sensor. Notice the difference in arrival times which allows the calculation of the speed of acoustic emission waves induced onto the aluminum or composite specimen. Table 1 tabulates the experimental data and the derived speeds of the ultrasonic waves in aluminum and the composite specimens.

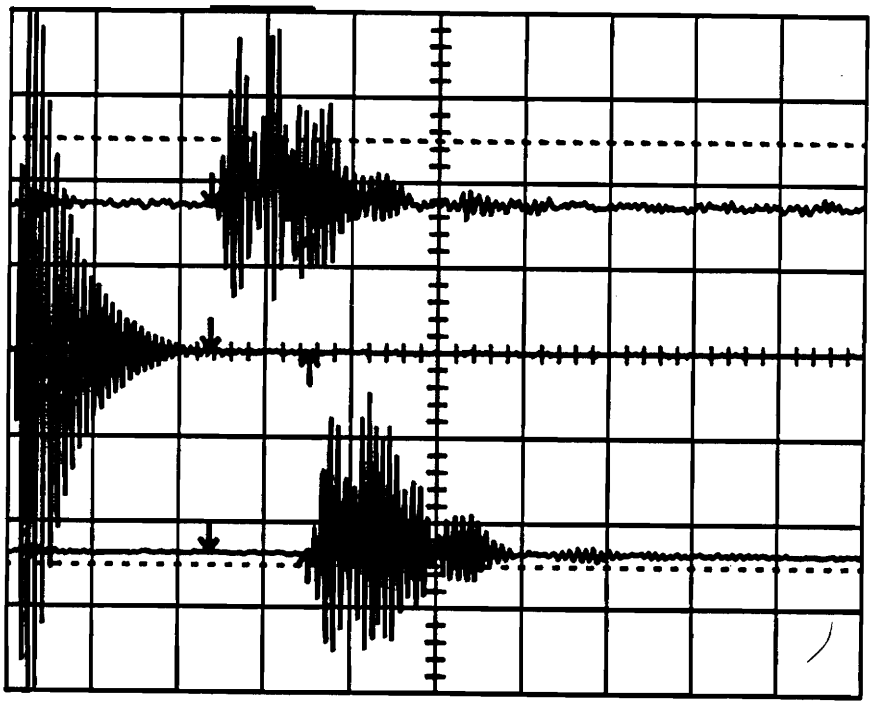

Figure 4.5. Response of the EFPI sensor at two different locations of the PZT.

To determine the wavelength of the surface acoustic waves in composite and the aluminum the sensor was interrogated with three different frequencies (1.2, 1.3 and 1.4 MHz). The frequencies were in the vicinity of 1.2 MHz because the piezoelectric transducer exhibited resonance at that frequency. The speed of the acoustic signals is dependent on the properties of the material through which it propagates and is independent of the frequency

of the acoustic emission. The wavelengths were calculated from the speeds derived in Table 1. Table 2 summarizes the obtained results.

Table 1. Comparison of surface acoustic wave speeds in aluminum and composite.

Material	Distance between the two source points	Difference in arrival times	Calculated speed
Aluminum	1 inch (2.54 cms)	8.75 μs	2903 m/s
Composite	1 inch (2.54 cms)	15.70 μs	1618 m/s

Table 2. Comparison of surface acoustic wavelengths in aluminum and composite.

Frequency of interrogation	Calculated wavelength in aluminum	Calculated wavelength in composite
1.2 MHz	2.42 mm	1.34 mm
1.3 MHz	2.23 mm	1.24 mm
1.4 MHz	2.07 mm	1.15 mm

Composites are nonisotropic in nature because of their crossed multilayer structure. This anisotropic property may result in the variation of surface acoustic wave speed on the direction with respect to the fibers in the composite. To study this effect, an experiment was conducted on a graphite-epoxy composite specimen 31 X 9.5 X 0.62 cm in dimensions. Three arcs were drawn on the panel each separated by 0.5 inches and they were divided into ten angles from 0° to 90° as shown in Fig. 4.4. One arc was used to

place the sensor and the other two arcs were used to place the PZT source that generates the surface acoustic waves. The time difference between the arrival times of the two signals due to the different locations of the PZT source were observed for different angles and the speeds were calculated. Table 3 summarizes the obtained results.

Table 3. Variation of SAW speed with respect to x axis.

Angle (degrees)	Time delay (μs)	Speed (m/s)
0	10.6	1198
10	11.8	1076
20	8.8	1443
30	11.6	1095
40	10.9	1165
50	10.9	1165
60	10.4	1221
70	11.2	1134
80	11	1154
90	8	1587

No variations in the speed of the SAW have been observed within an experimental accuracy in time delay of 3 μs. Anisotrpy of composites can be verified by measuring large time delays.

For ultrasonic attenuation in a polycrystalline engineering material, the attenuation consists of the sum of scattering by flaws, scattering by grains, absorption by various mechanisms,

beam spreading, and instrumental effects. The study of changes in ultrasonic velocity or attenuation with residual or applied stresses is known as acoustoelasticity.

Attenuation measurements were performed on the experimental setup shown in Fig. 4.4. A large aluminum plate was used to characterize the attenuation of SAW in aluminum. The large plate was used to eliminate back reflections from the ends of the aluminum plate which could cause an undesirable standing wave pattern. Initially the sensor was displaced with respect to the SAW source, which resulted in different sensing conditions for different readings. The response of the of the sensor largely depended on the amount of glycerin used on the sensor for efficient strain transfer.

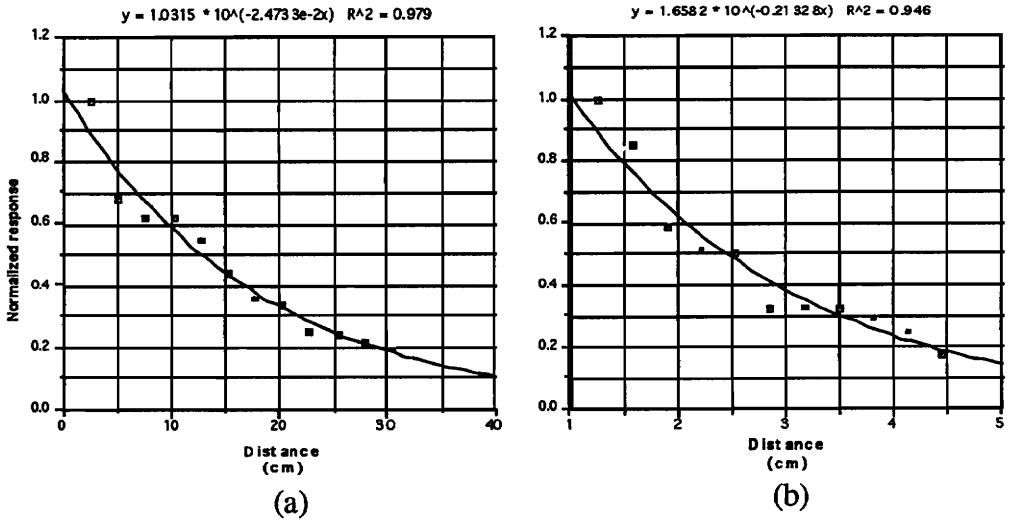

Figure 4.6. Attenuation curves for (a) aluminum (b) composite specimens.

Thus, it was decided to displace the source with respect to the sensor (keeping the sensing conditions intact), rather than the sensor with respect to the source. Fig. 4.6a shows the normalized response of the sensor versus the distance between the sensor and the source

for the aluminum specimen. The attenuation of the plane sinusoidal wave of small amplitude is exponential in nature and is given by

$$P(x) = P_o \exp(-\alpha x), \tag{4.1}$$

where P_O is the pressure amplitude at the origin, α is the attenuation coefficient and x is the distance from the sensor. Fig. 4.6b shows the attenuation curve for a composite specimen. The attenuation coefficients were calculated to be 0.06 cm^{-1} and 0.49 cm^{-1} for aluminum and composite materials respectively. Thus we conclude that the surface acoustic waves attenuate much faster in a composite panel than in aluminum. This is consistent with the theory that the attenuation coefficient of ultrasonic waves is inversely proportional to the velocity of propagation.

4.3 Directional sensitivity of an EFPI sensor

The response of the sensor to the direction of the source of the acoustic emission is important for qualitative detection of SAW and some applications such as impact location detection. Fig. 4.4 shows the experimental setup for the study of the directional response of the EFPI sensor to SAW. Lines were drawn from the center of a semicircle towards the circumference having a spacing of 5° on a section of the aluminum panel. The piezoelectric transducer mounted on the wedge was then placed at the intersection points of the lines and the circumference and tangential to the lines from the center of the semicircle. Ultrasonic signals were induced into the aluminum sample.

Several sensors with gage lengths equal to 1 cm were fabricated and tested for directional sensitivity. The output voltage (p-p) from the sensor was observed for the different angles

of the SAW source with respect to the sensor. Each observation was an average of one thousand samples. It was observed that the signal sensed by the EFPI sensor was not an exact replica of the exponentially decaying sinusoidal input pulse to the PZT, but a cosine amplitude modulated signal of the input pulse. This was attributed to the fact that the time taken by the input pulse to travel from one end of the EFPI sensor to the other end was comparable to the pulse width. To obtain a close match between the detected EFPI signal and the input pulse, the time taken by the pulse to traverse the EFPI sensor was made very small compared to the pulse width. This was achieved by fabricating sensors with gage lengths comparable to the wavelength of perturbation. Thus, an EFPI sensor was fabricated with a 2 mm gage length and tested for directional responsivity.

The EFPI sensor is sensitive only to the strain along the length of the sensor. The EFPI sensor has the minimum response when the gage length is an integer multiple of the wavelength and maximum response when the gage length is an integer multiple of the wavelength plus half the wavelength. Mathematically this can be represented by

$$\begin{aligned} G.L &= N\lambda, \text{ minimum response} \\ G.L &= N\lambda + \frac{\lambda}{2}, \text{ maximum response} \end{aligned} \qquad (4.2)$$

where G.L. stands for the gage length of the sensor, N is an integer and λ is the wavelength of the SAW in the medium. Using the above relation, a theoretical model can be developed for the response of the sensor. The figure below can be used to develop a model for the directional sensitivity of the EFPI sensor.

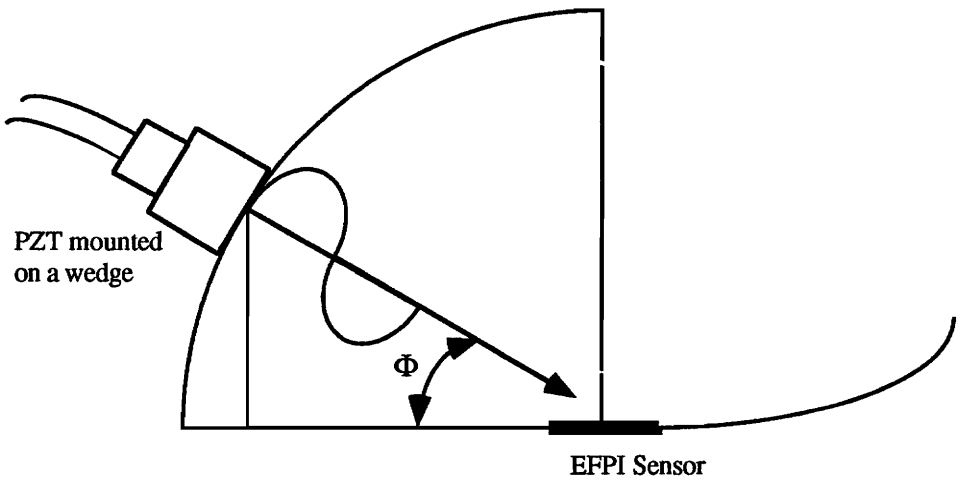

The EFPI sensor responds only to the strain along its longitudinal axis. Thus the EFPI sensor senses only the component of the input pulse along the sensor. As the EFPI sensor senses only the component along the longitudinal axis ($\lambda\cos(\Phi)$) of the sensor Equation 4.2 can be rewritten as

$$\frac{G.L.}{\lambda\cos(\Phi)} = N + y, \tag{4.3}$$

where y is the variable proportional to the response and varies between 0 and 1. The response of the sensor is minimum when y = 0 and maximum when y = 0.5 and when y is greater than 0.5 the response of the sensor is given by 1- y. Even though variable y gives the response of the sensor, it does not consider the component of the amplitude of the SAW sensed by the sensor which varies as $\cos(\Phi)$. Thus the complete response of the sensor is given by $y\cos(\Phi)$. A computer program was written to calculate the response of the sensor. Fig. 4.7 shows the theoretical and practical curve for the EFPI sensor. There is an excellent agreement between the measured and calculated curves.

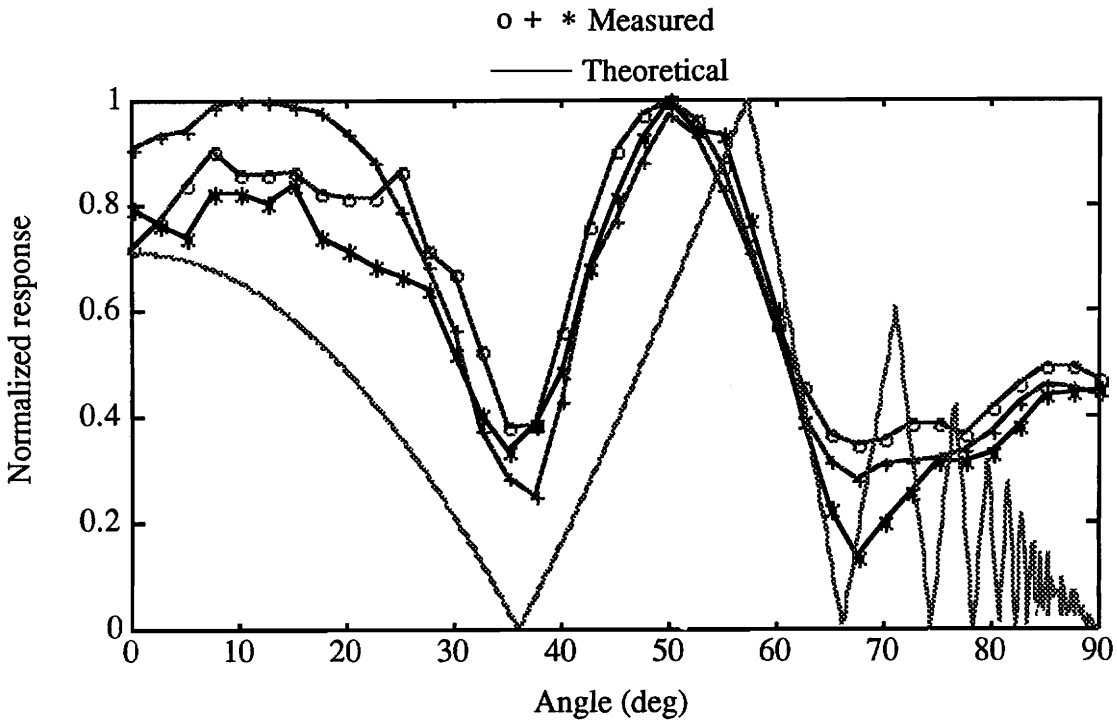

Figure 4.7. Directional sensitivity of an EFPI sensor to SAW.

Chapter 5 - Conclusions and future directions

5.1 Conclusions

A noncontact hybrid interferometer has been demonstrated for measuring absolute amplitudes of surface acoustic waves (SAW). Calibration of the piezoelectric transducer (PZT) cylinder has been performed using the J1..J4 spectrum analysis technique. A phase shifting coefficient (PSC) of 2.26 rad/V has been measured for the PZT cylinder. The J0/J2 spectrum analysis technique is used for demodulating the SAW signal from the interferometer. Phase shifts of 5 - 30 mrads corresponding to SAW amplitudes of 5 - 15 A° have been measured.

A broadband preamplifier was designed to replace the avalanche photodiode used in the interferometer. The system was designed with a bandwidth of 1.5 MHz and the sensitivity of the system was measured to be 0.82 V/μW. Theoretical and practical minimum detectable air gap change for an EFPI were calculated to be 1.2 A° and 35 A° respectively. Better minimum detectable air gap changes can be achieved by improving the detection

electronics. An improvement would be to design a tunable broadband preamplifier to reduce the noise.

Several EFPI sensors were fabricated for use in material characterization tests. Pencil lead tests were performed to simulate acoustic emission in a composite specimen to determine their frequency range. It was observed that the acoustic emission frequencies were in the range 20 - 500 kHz. Also, consistent results were obtained for different pencil lead break tests on the graphite bismalliumuth composite specimen. While there was no difference in the acoustic emission frequency range for the 0.5 and 0.7 mm pencil fractures, however, the average magnitude of the frequency peaks was higher for the 0.7 mm pencil lead fracture. This could be due to the greater amount of force required to break a thicker pencil is more.

SAW speeds were measured on aluminum and composites. SAW speeds were calculated to be 2903 and 1618 m/s. It was observed that the speed of SAW is greater in aluminum than in composite specimen. This is due to the morphology of the graphite present in the composite specimen. The ultrasonic velocity varies with average graphite morphology fairly linearly over its linear range [4.5]. Also the graphite morphology is a function of the strength of the material, thus making the study of speed measurements in materials more important.

Attenuation coefficients of 0.06 and 0.49 cm^{-1} were measured for aluminum and composite specimens. The attenuation is greater in the composite specimen roughly by a factor of 10. This is due to the amount of scattering of ultrasonic waves in composite materials. Ultrasonic scattering is dependent upon several factors such as frequency, grain size, grain size distribution, crystallographic anisotropy and microstructure. Thus, a family

of measurements will be necessary to correlate the attenuation coefficients to the material property.

5.2 Future directions

The experimental results presented have clearly demonstrated the use of optical fiber sensors in nondestructive evaluation of materials. Significant improvements can be made in the detection and quantitative measurements of low amplitude acoustic emission signals with the inclusion of

- better detection electronics to improve the signal to noise ratio of the system,
- better signal detection schemes to increase the minimum detectable phase shift, and
- better sensor designs.

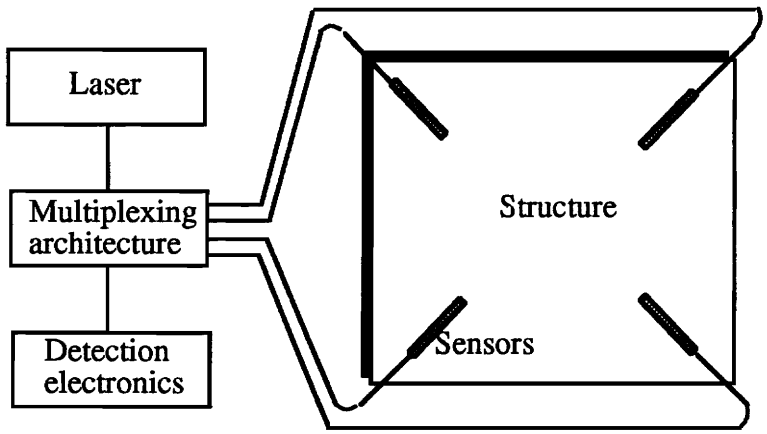

Figure 5.1. A structure incorporating multiplexed EFPI sensors.

Optical fiber sensors can be used in the acousto-ultrasound approach for NDE to detect cracks and crack propagation. Fiber sensors can be embedded into the material during their fabrication. An array of sensors embedded in the material or a structure can be used for

studying various material properties and damage detection. Fig. 5.1 illustrates a system incorporating several EFPI sensors. A single laser can be used as a source for several sensors. Various multiplexing architectures can be used depending on the parameters to be measured by the sensors. Such a system can be used to detect cracks, structural damages, impacts and to predict impact locations.

References

[1.1] R. Halmshaw, Nondestructive Testing, Metallurgy and Material Science series. Edward Arnold publishers Ltd., USA, 1987.

[1.2] M. Purschke and M. Schaefer, "Fully Automated X Ray Testing of Cast Parts" , *Proc. of 13th World Conf. on NDT*, Sao Paulo, Brazil, 1992, pp. 572-578.

[1.3] H. T Hahn , "Application of Ultrasonic techniques to Cure Characterization of epoxies," Nondestructive methods for material property determination, Plenum Press, New York and London 1984, pp. 315-326.

[1.4] A. Vary, "The acousto-ultrasonic approach," Acousto-ultrasonic: Theory and Applications, Plenum Press, New York and London 1988, pp. 1-21.

[1.5] A. M. Aindow, R. J. Dewhurst, and S. B. Palmer, "Laser Generation of Directional Acoustic Surface Wave Pulses in Metals," *Optics Communications*, Vol. 42, 1982, p. 116.

[1.6] Hsu. N, Acoustic emission simulator US Patent 4018084 assigned to Lockheed Aircraft Corp., Burbank, California, May 1976.

[1.7] S. Rudraraju, R. O. Claus, and K. A. Murphy, "Comparison of Optical Fiber and Piezoelectric Methods for the Detection of Acoustic Waves", *Symposium on Adaptive Structures and Material Systems*, ASME Winter Annual Meeting, Nov. 29-30, 1993.

[1.8] Vary. A, Bowler. K. J, "An Ultrasonic-acoustic Technique for NDE of Fiber Composite Quality," *Polymer Engineering and Science* , no. 19, 1979, p.373.

[2.1] Eric Udd, "The emergence of fiber optic sensor technology," Fiber Optic Sensors: An Introduction for Engineers and Scientists, John Wiley & Sons Inc., 1991, pp. 1-8.

[2.2] Peter Raiti, "Fiber Optic Sensors for Smart Skins Applications," *Society for photonic and instrumentation engineers*, Vol. 1370, 1990, pp. 6-19.

[2.3] Thomas. G. Giallorenzi, Joseph. A. Bucaro, Anthony Dandridge, G. H. Sigel, Jr., James H. Cole, Scott. C. Rashleigh and Richard. G. Priest, "Optical Fiber Sensor Technology," *IEEE Journal of Quantum Electronics*, Vol. QE-18, no. 4, April 1982, pp. 626-665.

[2.4] Shi-Kay Yao and Charles K. Asawa, "Fiber Optical Intensity Sensors," *IEEE Journal on Selected Areas in Communications*, Vol. SAC-1, no 3, April 1983, pp. 562-575.

[2.5] D. A. Krohn, Fiber Optic Sensors and Applications, Instrumentation Society of America, 1992.

[2.6] J. P. Dakin and D. A. Kahn, "A novel Fiber-Optic Temperature Probe," *Opt. Quantum Electronics*, Vol. 9, 1977, pp. 540-544.

[2.7] J. H. Lyle, and C. W. Pitt, "Vortex Shedding Fluid Flowmeter Using Optical Fiber Sensor," *Electronic Letters*, Vol. 17, 1981, p.244.

[2.8] S. K. Yao, C. K. Asawa, and G. F. Lipscomb, "Microbending Loss in a Single Mode Fiber in the Pure-Bend Loss Regime," *Applied Optics*, Vol. 21, 1982, p. 3059.

[2.9] D. A Jackson, "Monomode Optical Fiber Interferometers for Precision Measurements," *Journal of Physics*, E:Sci. and Instrum., Vol. 18, 1985, pp. 981-1001.

[2.10] Moss. G. E, Miller L. R, and Forward R. L, "Photon-Noise Limited Laser Transducer for Gravitational Antenna," *Applied Optics*, Vol. 10, 1971, p. 2495.

[2.11] A. Dandridge, A. B. Tveten, and T. G. Giallorenzi, "Homodyne Demodulation Scheme for Fiber Optic Sensors Using Phase Generated Carrier," *IEEE Journal of Quantum Electronics*, QE-18, 1982, 1647.

[2.12] Yoshno. T, Kurosawa. K, Itoh. K, and Ose. T, "Fiber Optic Fabry-Perot Interferometer and its Applications," *IEEE Journal of Quantum Electronics*, QE-18, 1982, pp. 1624-1632.

[2.13] R. O. Claus, M. F. Gunther, A. Wang and K. A. Murphy, "Extrinsic Fabry-Perot Sensor for Strain and Crack Opening Displacement Measurements form - 200 to 900 °C," *Smart Materials and Structures*, Vol. 1, 1992, pp. 237-242.

[3.1] R. Williams, Acoustic Emission, Adam Higler Ltd., Bristol, England, 1980.

[3.2] H. N. G. Wadley, "Acoustic Emission: Nature's Ultrasound," Review of Progress in Quantitative Nondestructive Evaluation, Vol. 5A, Plenum Press, New York, 1985.

[3.3] Tuan. A. Tran, "Extrinsic Fabry-Perot Interferometer for Surface Acoustic Wave Measurements," Virginia Polytechnic Institute and State University, Virginia, 1991.

[3.4] Anthony Dandridge, "Fiber Optic Sensors Based on the Mach-Zehnder and Michelson Interferometers," Fiber Optic Sensors: An Introduction for Engineers and Scientists, John Wiley & Sons Inc., 1991, pp. 271-323

[3.5] V. S. Sudarshanam and K. Srinivasan, "Linear Readout of Dynamic Phase Change in a Fiber-Optic Homodyne Interferometer," *Optics Letters*, Vol. 14, 1989, pp. 140-142.

[3.6] V. S. Sudarshanam, "New Spectrum Analysis Technique for Interferometric Vibration Measurement," *Optics Communications*, Vol. 88, 1992, pp. 291-294.

[3.7] C. Harvey Palmer, Richard. O. Claus, and Steven E. Fick, "Ultrasonic Wave Measurement by Differential Interferometry," *Applied Optics*, Vol. 16, no 7, 1977, pp. 1849-1856.

[4.1] Tran. T. A, Miller. K. A., Vengsarkar A. M. and Claus. R. O, "Stabilized Extrinsic Fiber-Optic Fizeau Sensor for Surface Acoustic Wave Detection," *Journal of Lightwave Technology*, Vol. 10, no. 10, 1992.

[4.2] Gunther. M. F, Wang. A, Fogg. B. R, Starr. S. E, Murphy. K. A, and Claus. R. O, "Fiber Optic Impact detection and Location system Fmbedded in a Composite Material," *SPIE 3/FIBER*, Boston MA, Sept. 8, 1992.

[4.3] J. Sirkis, "Phase-Strain-Temperature Model for Structurally Embedded Interferometric Optical Fiber Strain Sensors with Applications," *SPIE*, Vol. 1588, 1991, pp. 26-43.

[4.3] Ian G. Scott, Basic Acoustic Emission, Gordon and Breach Science Publishers, Switzerland, 1991.

[4.4] "The EWGAE Code for AE-location of Sources of Discrete Events," NDT International, Aug. 1981, p. 181.

[4.5] Emmanuel P. Papadakis , "The Inverse Problem in Material Characterization Through Ultrasonic Attenuation and Velocity Measurements," Nondestructive methods for material property determination, Plenum Press, New York and London 1984, pp. 151-160.

Vita

Sridhar Rudraraju was born in the city of Hyderabad, India on February 17, 1970. He graduated with a Bachelor of Engineering degree in Electronics Engineering from the Motilal Nehru Regional Engineering College, Allahabad in May 1991. He enrolled in Virginia Polytechnic Institute and State University's Graduate School Program in Electrical Engineering in August 1991. During his graduate career he was employed as a Graduate Research Assistant by the Fiber and Electro-Optics Research Center. He completed his Master of Science degree in Electrical Engineering in 1994.

His professional interests include optical fiber sensing and communications. He is a member of the Institute of Electrical and Electronics Engineers.